Article

Composites Based on Poly(ortho-toluidine) and WS$_2$ Sheets for Applications in the Supercapacitor Field

Teodora Burlanescu [1,2], Ion Smaranda [1], Andreea Androne [1], Cristina Stefania Florica [1], Madalina Cercel [1], Mirela Paraschiv [1], Adelina Udrescu [1], Adam Lőrinczi [1], Petru Palade [1], Andrei Galatanu [1], Catalin Negrila [1], Elena Matei [1], Monica Dinescu [1], Radu Cercel [1] and Mihaela Baibarac [1,*]

[1] National Institute of Materials Physics, Atomistilor Street 405A, 077125 Bucharest, Romania; teodora.burlanescu@infim.ro (T.B.); ion.smaranda@infim.ro (I.S.); andreea.radu@infim.ro (A.A.); stefania.florica@infim.ro (C.S.F.); madalina.chivu@infim.ro (M.C.); mirela.cristea@infim.ro (M.P.); adelina.udrescu@infim.ro (A.U.); lorinczi@infim.ro (A.L.); palade@infim.ro (P.P.); gala@infim.ro (A.G.); catalin.negrila@infim.ro (C.N.); elena.matei@infim.ro (E.M.); monica.daescu@infim.ro (M.D.); radu.cercel@infim.ro (R.C.)

[2] Faculty of Physics, University of Bucharest, Atomistilor Street 405, 077125 Bucharest, Romania

* Correspondence: barac@infim.ro

Abstract: In this work, three methods for the synthesis of composites based on poly(ortho-toluidine) (POT) and WS$_2$ are reported: (a) the solid-state interaction (SSI) of POT with WS$_2$ nanoparticles (NPs); (b) the in situ chemical polymerization (ICP) of ortho-toluidine (OT); and (c) the electrochemical polymerization (ECP) of OT. The preparation of WS$_2$ sheets was performed by the ball milling of the WS$_2$ NPs followed by ultrasonication in the solvent N,N'-dimethyl formamide. During the synthesis of the POT/WS$_2$ composites by SSI and ICP, an additional exfoliation of the WS$_2$ NPs was reported. In this work, we demonstrated the following: (a) the ICP method leads to POT/WS$_2$ composites, which contain repeating units of POT in the leucoemeraldine salt (LS) state, while (b) the ECP method leads to POT/WS$_2$ composites, which contain repeating units of POT in the emeraldine salt (ES) state. Capacitances equal to 123.5, 465.76, and 751.6 mF cm^{-2} in the cases of POT-ES/WS$_2$ composites, synthesized by SSI, ICP, and ECP, respectively, were reported.

Keywords: composites; conducting polymers; transition metal dichalcogenides; sheets; Raman scattering; FTIR spectroscopy; cyclic voltammetry; supercapacitors; energy storage

1. Introduction

Composites based on conducting polymers and transition metal dichalcogenides (TMDs) have been of particular interest as a result of applications in the fields of photocatalysis [1], gas sensors [2], and, last but not least, supercapacitors [3–5]. The methods often used for the synthesis of polyaniline (PANI)/WS$_2$ composites are as follows: (i) the method of the chemical interaction of nanolayers of WS$_2$ with PANI in a solid state [3]; (ii) the ECP of a monomer in an anhydrous solution of H$_2$SO$_4$, acetonitrile, and WS$_2$ microparticles [4]; and (iii) the exfoliation of WS$_2$ microparticles in butyl lithium, followed by the ICP of aniline [6]. The use of TMDs in the bulk state in supercapacitors (SCs) has often been avoided due to their small surface area (SA). The large SA of individual TMD sheets and higher oxidation numbers (e.g., in MoS$_2$ from +2 to +4) allow TMDs to store electrostatic charge as well as ionic interlacing in the interlayer space, leading to a specific capacitance and an energy density with higher values [7,8]. The main methods for TMD exfoliation are as follows: (a) mechanically; (b) in the liquid phase, using organic solvents or surfactants;

(c) ion intercalation; and (d) grinding [9]. Concerning the particular case of WS_2 nano- and microparticles, among the main strategies adopted for the exfoliation of these TMDs are (i) liquid-phase exfoliation assisted by the ultrasonication of the WS_2 crystals in surfactant aqueous solutions [10] or organic solvents [11] as well as superacid (chlorosulfonic acid) [12]; (ii) chemical exfoliation performed in three stages involving magnetic stirring, horn-tip sonication, and shear mixing [13]; (iii) electrochemical exfoliation at a DC potential of 10 V [14]; (iv) solvothermal reaction [15], etc. The methods often used to illustrate TMD exfoliation are X-ray diffraction (XRD), scanning electron microscopy (SEM), Raman scattering, and X-ray photoelectron spectroscopy (XPS), e.g., in [10–15]. A disadvantage of liquid-phase exfoliation assisted by the ultrasonication of WS_2 crystals is the long time taken to obtain the nanolayers as a consequence of the successive ultrasonication and centrifugation stages. In this work, special attention will be paid to obtaining WS_2 sheets by grinding WS_2 NPs followed by ultrasonication for a short period in N,N′-dimethyl formamide (DMF).

The low conductivity in the most stable phases of TMDs prevents their use as potential electrode materials in supercapacitor cells. Conductive polymers such as PANI [16] are often used in the field of supercapacitors as a result of their high specific capacitance, electrical conductivity >0.001 S/cm, manufacturing methods that do not require expensive equipment and high flexibility, ability to be obtained in different oxidation states such as leucoemeraldine, emeraldine, and pernigraniline, which correspond to reduced, semi-oxidized and oxidized states, and obtaining of polymers in undoped and doped states, respectively [17]. The following methods have been used to synthesize PANI/WS_2 composites: (i) the ICP of aniline using WS_2 sheets resulting from the exfoliation of WS_2 powder in water/isopropanol mixtures [18]; (ii) the interaction of the two constituents, e.g., in [3,19]; and (iii) the ECP of WS_2 dispersed in a mixture of aniline and acid solution, e.g., in [4]. According to Ref. [20], a disadvantage of PANI is its rigid structure, which can influence the capacitance of supercapacitors. An improvement in the processability of PANI was reported by replacing aniline with ortho-substituted aniline, with functional groups of the types -CH_3, -OCH_3, etc. [21]. One of the important properties of POT is its conductivity, which varies between 10^{-4} and 2×10^{-2} S/cm [22,23]. In this study, our effort will be given to the synthesis of composites based on WS_2 and POT and the evaluation of their optical, structural, and electrochemical properties. The following strategies will be used for the synthesis of POT/WS_2 composites: (i) the SSI of POT with WS_2 NPs; (iii) the ICP of ortho-toluidine (OT) with the addition of WS_2 NPs; and (iii) the ECP of OT in a semi-aqueous acid solution containing WS_2 sheets in DMF/H_2O (the volumetric ratio was 1:1). Using correlated studies of XRD and SEM, new evidence concerning the exfoliation of WS_2 NPs in the absence and presence of POT will be shown. The chemical interactions at the interface of the two constituents of the POT/WS_2 composites will be highlighted by Raman scattering, FTIR spectroscopy, and X-ray photoelectron spectroscopy (XPS). Using cyclic voltammetry (CV), new information concerning the capacitive and diffusion-controlled intercalation processes and their contributions to the current densities of cyclic voltammograms of the symmetrical supercapacitor cells that have electrodes containing the POT/WS_2 composites as active materials will be shown. An assessment of the dependence of the capacitance of the symmetrical supercapacitors as a function of the potential scan rate and cyclic voltammogram number will also be reported.

2. Materials and Methods

The supplier for the compounds OT, H_2SO_4, DMF, $K_2Cr_2O_7$, NH_4OH, CH_3CN, poly(vinylidene fluoride) (PVDF), dibutyl phthalate (DBP), acetone, diethyl ether, Nafion 117 membrane, and WS_2 NPs was Sigma-Aldrich (St. Louis, MO, USA).

To prepare the WS_2 sheets, a powder containing WS_2 NPs was used, which were subjected to mechanical exfoliation using a ball mill model PM 100—RETSCH and SamplePrep 8000 M shaker mill from SPEX, USA. Using the first ball mill, 1 g of WS_2 NPs was subjected to a grinding time of one hour at 150, 300, and 600 rpm. With the second mill, the grinding of 1 g of WS_2 NPs was carried out for an hour of effective milling time at 900 cycles/min. Milling periods of 5 min were interspersed with 5 min pauses to avoid excessive heating of samples. The changes induced in the crystalline structure of the WS_2 NPs by the exfoliation process were analyzed by XRD. An additional exfoliation after grinding WS_2 NPs for one hour at 900 rpm was performed by ultrasonicating a suspension of WS_2 in DMF for 15 min, leading to a yellowish solution with a concentration of 0.5 mg/mL.

The chemical synthesis of poly(o-toluidine)–emeraldine salt (POT-ES) and poly(o-toluidine)–emeraldine base (POT-EB) involved the use of two solutions of OT 0.18 M and $K_2Cr_2O_7$ 0.05 M, each in 50 mL H_2SO_4 2M. Adding the solution of $K_2Cr_2O_7$ in H_2SO_4 to the solution of OT in H_2SO_4 induces a change in the reaction mixture color from orange to dark green. After two hours, the chemical polymerization reaction led to a green precipitate, which corresponds to POT-ES. The filtration of POT-ES and its interaction with 1 M NH_4OH solution led to obtaining POT-EB, when a change in the color of the precipitate to dark blue occurred. Further, the interaction with 500 mL of distilled water and 100 mL of CH_3CN allowed the removal of oligomers from the reaction product. The polymerization reaction products, i.e., POT-ES and POT-EB, were dried at room temperature for 24 h to constant mass.

The ICP of the POT/WS_2 composites, having TMD concentrations of 20 wt.% and 10 wt.%, was performed as described above; the only difference was the addition of 0.1 g and 0.01 g of WS_2 NPs to the OT solution in H_2SO_4.

Another method for the preparation of the POT-EB/WS_2 composites was the SSI of POT-EB with WS_2 NPs when the TMD concentration in the composite mass was equal to 33 wt.% and 50 wt.%.

Electrochemical synthesis of POT-ES involves the use of a semi-aqueous solution of OT 0.1 M in H_2SO_4 0.5 M with a volumetric ratio of DMF/H_2O equal to 1:1.

The electrosynthesis of the POT-ES/WS_2 composite involved the preparation of (i) a WS_2 solution in DMF (50 mL, 0.5 mg/mL) by ultrasonication of the TMD in DMF for 15 min and (ii) an aqueous solution of 0.1 M OT in 0.5 M H_2SO_4 (50 mL). Subsequently, the solutions were interacted and homogenized by ultrasonication for 5 min. The reaction mixture was placed in a single-compartment cell, which was accessorized with three electrodes as follows: a Pt working electrode with an area of 1 cm^2, an auxiliary electrode made of Pt, and a Ag/AgCl reference electrode. Cyclic voltammograms were recorded in the potential range (-200; +900 mV) vs. Ag/AgCl at a potential scan rate of 50 mV/s, with a Voltalab 80 potentiostat/galvanostat, purchased from Radiometer Analytical.

XRD diagrams of the POT/WS_2 and POT-ES/WS_2 composites were recorded with Bruker's D8 Advance X-ray diffractometer (Bruker, Hamburg, Germany).

The SEM images of WS_2 NPs before and after exfoliation as well as their composites with POT-EB were recorded with the Zeiss Gemini 500 scanning electron microscope (Zeiss, Oberkochen, Germany).

The Raman spectra of WS_2, POT-EB, POT-ES, and the POT-ES/WS_2 and POT-EB/WS_2 composites were recorded using an FTRaman spectrophotometer, MultiRam model, from Bruker (λ_{exc} = 1064 nm, (Ettlingen, Germany)).

To record IR spectra of POT-EB, POT-ES, and the POT-ES/WS_2 and POT-EB/WS_2 composites, we used an FTIR spectrophotometer, model Vertex 80, from Bruker (Billerica, MA, USA), in the transmission geometry mode for compounds prepared by SSI and ICP, while for composites deposited as films on the Pt electrode, the totally attenuated reflection geometry was used.

To record the UV-VIS spectrum of WS_2 sheets, we used a Lambda 950 UV-VIS-NIR spectrophotometer from Perkin-Elmer (PerkinElmer, Inc., Waltham, MA, USA).

The XPS spectra of WS_2, POT-EB, POT-ES, and the POT-ES/WS_2 and POT-EB/WS_2 composites were recorded on a SPECS spectrometer (SPECS Gmbh, Berlin, Germany) with a Phoibos 150 electron energy analyzer and a monochromatic X-ray source of the type Al $K\alpha$ 1486.74 eV.

The testing of composites as electrode active materials (EAMs) in SC cells was performed by CV. To prepare electrodes, we used a mixture of 80 wt.% EAM, 5 wt.% PVDF, 15 wt.% super-P conductive black carbon, 0.1 mL DBP, and 1 mL acetone, which were mixed for 12 h under magnetic stirring to obtain a homogeneous paste. A film was obtained after the evaporation of the acetone from the paste poured onto the glass slides. To remove DBP from the film to be used as an electrode in SCs, an interaction with diethyl ether was performed. The electrodes for SC cells were in a circular form with a diameter of 8 mm obtained by cutting above the film. The electrolyte used in the SC study was a Nafion 117 membrane treated with a 1 M H_2SO_4 solution [21].

3. Results and Discussion

3.1. Exfoliation of the WS_2 Nanoparticles as Well as Their Optical and Structural Properties

Figure 1(a_1,a_2) show SEM images of WS_2 flakes. According to Figure 1(a_2), WS_2 flakes have a diameter between 260 and 460 nm and a width between 30 and 78 nm. Figure 1 shows that the thinnest WS_2 sheets were obtained when the grinding of WS_2 flakes took place at 900 rpm for one hour.
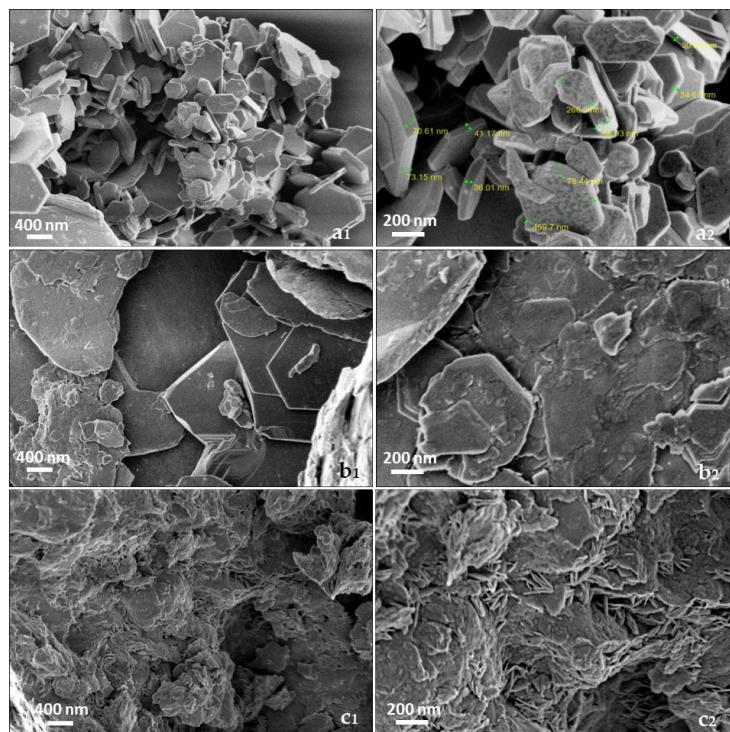
Figure 1. SEM images of WS_2 flakes (a_1,a_2); the WS_2 nanosheets resulting from grinding flakes for one hour at 600 rpm (b_1,b_2) and 900 rpm (c_1,c_2).

Figure 2 shows an SEM image of the WS_2 sheets deposited onto the Si plate after the evaporation of DMF from the solution prepared using WS_2 sheets, resulting from grinding flakes for one hour at 900 rpm, and then its dispersion by ultrasonication in DMF.
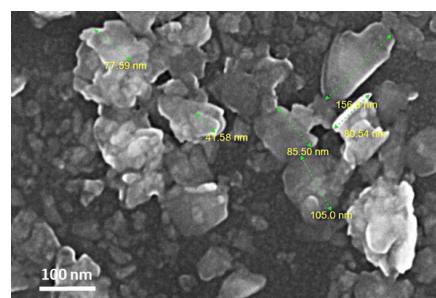
Figure 2. SEM image of WS$_2$ sheets.

Figure 2 shows WS$_2$ sheets of various sizes, some of which are rolled.

Information confirming the formation of WS$_2$ sheets is presented by XRD in Figure 3. Figure 3a shows the XRD diagram of WS$_2$ nanoparticles, where diffraction maxima are observed at 2θ angles of cca. 14.3°, 28.8°, 32.8°, 33.5°, 39.6°, 43.9°, 49.7°, 58.4°, 59.8°, and 60.3°, belonging to the crystalline planes (002), (004), (100), (101), (103), (006), (105), (110), (008), and (112) [PDF 00-008-0237]. An important detail highlighted in Figure 3a is that the peak intensity of the crystalline plane (002) is 3.58×10^5 counts. According to Figure 3c, it is observed in the XRD diagram that mechanical exfoliation induces a significant decrease in the intensity of the maximum corresponding to the crystal plane (002) to cca. 6.53×10^3 counts, accompanied by a diminution in the intensity of the maxima corresponding to the crystalline planes (004), (006), and (008).

(**a**)


(**b**)

Figure 3. *Cont.*

(c)
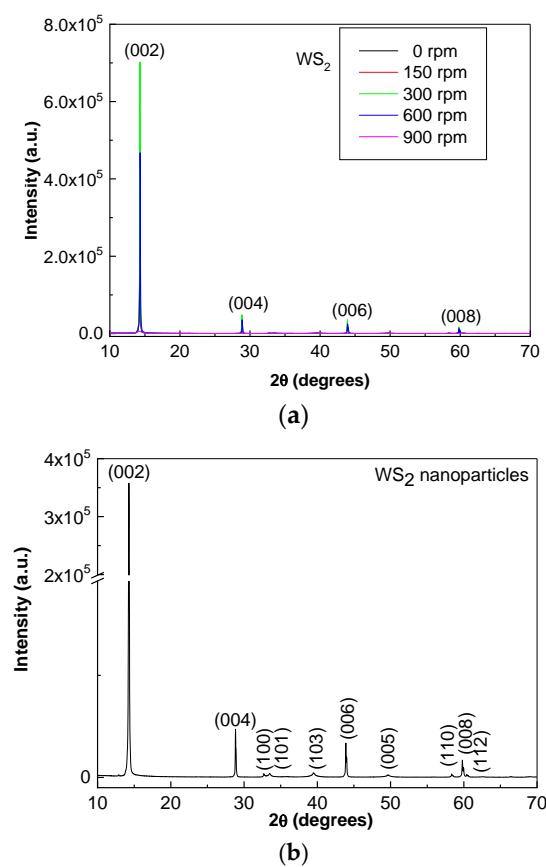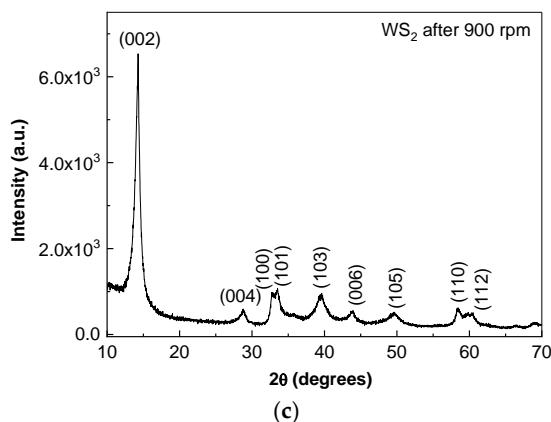
Figure 3. (**a**) XRD diagrams of WS$_2$ nanoparticles before and after grinding at 150, 300, 600, and 900 rpm. (**b,c**) X-ray diagrams of WS$_2$ nanoparticles before and after 900 rpm.

These variations are typical for the exfoliation of WS$_2$ particles, and to support this claim, an example may be the case of exfoliation of WS$_2$ particles mixed with lithium halides [24] or organic solvents such as ethanol, acetone, methanol, isopropyl alcohol, dimethyl formamide, and N-methyl pyrrolidone [24].

The Raman spectra of WS$_2$ NPs before and after their exfoliation are shown in Figure 4. According to Figure 4a, two intense Raman lines of WS$_2$ NPs with maxima of 357 and 422 cm^{-1} are observed. These are attributed to the E$_{2g}$^{1} and A$_{1g}$ vibrational modes, respectively, that must be understood as related to in- and out-of-plane vibrations of W and S atoms [25].


(a)　　　　　　　　　　　　　　　　　(b)
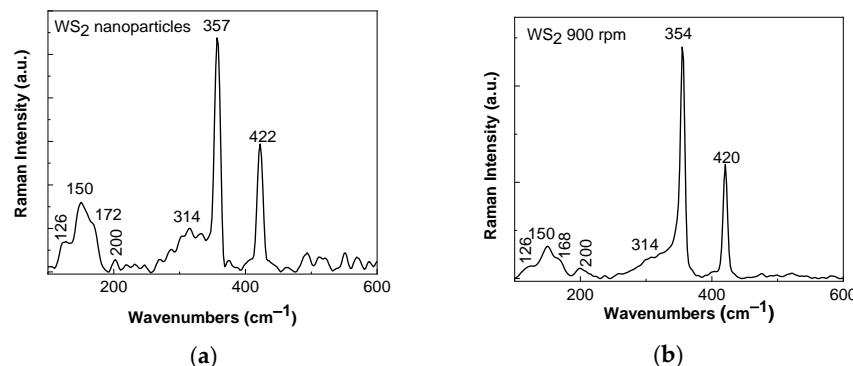
Figure 4. The Raman spectra of WS$_2$ NPs before (**a**) and after grinding exfoliation at 900 rpm (**b**).

Raman lines at 126, 168–172, and 314 cm^{-1} were assigned to the vibrational modes A$_g$, B$_u$, and A$_g$ of 1T'-WS$_2$ [26]. The Raman line at 200 cm^{-1} belongs to the vibrational mode E''(M) - ZA(M) [27]. The Raman line that peaks at 150 cm^{-1} is situated no longer in terms of wavelength than that reported at 148 cm^{-1}, which is characteristic of monolayer WS$_2$ [28]. In Figure 4b, we can observe two Raman lines of WS$_2$ sheets associated with vibrational modes E$_{2g}$^{1} and A$_{1g}$, which show a shift at cca. 354 and 420 cm^{-1}, which has been attributed to the exfoliation of WS$_2$ microparticles [24]. In the context of the exfoliation process of WS$_2$ NPs, an important parameter is the distance between the two Raman lines associated with vibrational modes E$_{2g}$^{1} and A$_{1g}$ and the ratio between their intensities (I$_{Eg}$/I$_{Ag}$). Careful analysis of Figure 4a,b reveals that (a) the distance between the Raman lines associated with vibrational modes E$_{2g}$^{1} and A$_{1g}$ is equal to 65 and 66 cm^{-1}, respectively, and (b) the I$_{Eg}$/I$_{Ag}$ ratio is equal to 1.8 and 1.1, respectively.

The UV-VIS spectrum of WS$_2$ sheets mechanically exfoliated at 900 rpm, which were further dispersed into DMF by ultrasonication for 15 min (Figure 5), shows a band at

632 nm, accompanied by another band presenting one shoulder at 530 nm and another one at 454 nm, which were attributed to the exciton band, the transition of the indirect exciton, and the optical transition between the valence and conduction bands specific to the semiconductor character of the direct forbidden band [29].
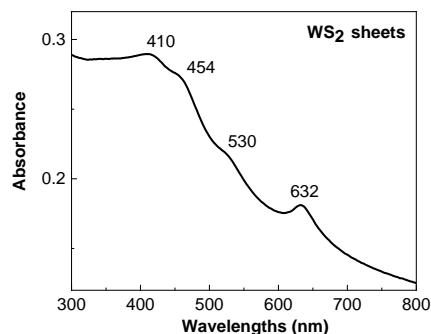
Figure 5. UV-VIS spectrum of WS_2 sheets resulting from mechanical exfoliation at 900 rpm, followed by ultrasonication in DMF.

3.2. POT/TMD Composites Obtained by SSI and ICP

According to Figure 6a, the SSI of the constituents of the POT-EB/WS_2 composite involves the exfoliation of WS_2 nanoparticles, which was evidenced in the XRD by decreasing the peak intensity of the crystal planes (002) from 6.35×10^5 counts/sec (black curve in Figure 6a) to 3.58×10^5 counts/sec (blue curve in Figure 6a) to 1.11×10^5 counts/sec (red curve in Figure 6a).

(a)

(b)
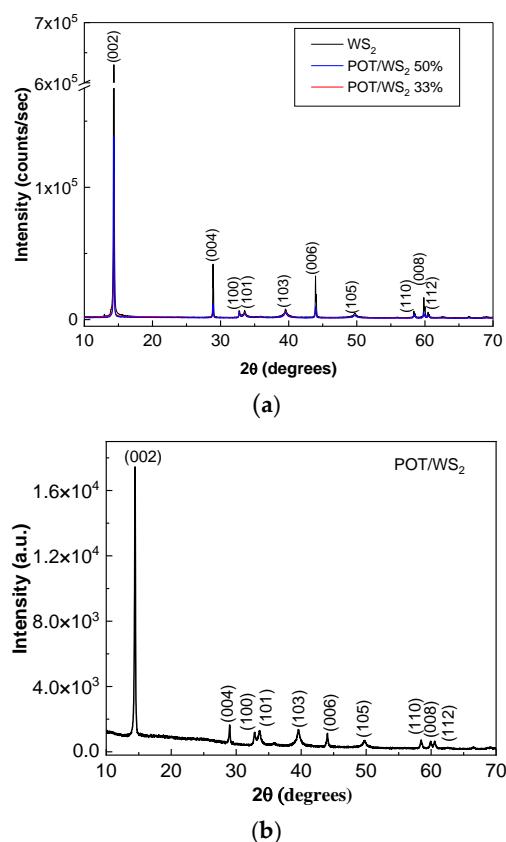
Figure 6. (**a**) XRD diagrams of WS_2 NPs (black curve) and the POT-EB/WS_2 composites obtained by SSI, when the WS_2 concentration in the composite mass is 50 wt.% (blue curve) and 33 wt.% (red curve). (**b**) XRD diagram of POT/WS_2 composite obtained by ICP of OT, when the WS_2 concentration in the composite mass is 20 wt.%.

This exfoliating process of WS$_2$ nanoparticles is also observed in the ICP of OT assisted by WS$_2$ NPs. In this context, the diffraction peak intensity of the crystalline plane (002) of WS$_2$ varies from 6.35×10^5 counts/sec (black curve in Figure 6a) to 1.74×10^4 counts/sec (Figure 6b) for the sample with a WS$_2$ concentration equal to 20 wt.% in POT-EB/WS$_2$ composite mass.

The analysis of Figure 7a,b indicates that Raman spectra of the POT-EB and POT/WS$_2$ composite show Raman lines that belong to (a) WS$_2$, these being situated at 359 and 421 cm^{-1}, and (b) POT, these being localized at 1119, 1176, 1259, 1329–1363, 1499, and 1620 cm^{-1} and attributed to the vibrational modes of deformation of the benzene ring (B) + C-H bond in the CH$_3$ group, the C-H bond in B, the stretching C-N bond + stretching C-C + C-H bonds in B, the stretching C-C bond in B, the stretching C-C bond in the quinoid ring (Q) + C-H bond in B, and the stretching C-N bond and stretching C-C + C-H bond in B [30,31]. The Raman lines at 1119, 1259, 1363, and 1620 cm^{-1} are closely situated to those reported in the POT-EB (Figure 7a) that peaked at 1117, 1254, 1367, and 1618 cm^{-1}. In contrast with the Raman line of POT-EB at 1163 cm^{-1} (Figure 7a), the Raman line of the POT/WS$_2$ composite is situated at 1176 cm^{-1} (Figure 7b) as a consequence of the generation of POT–emeraldine salt (ES).
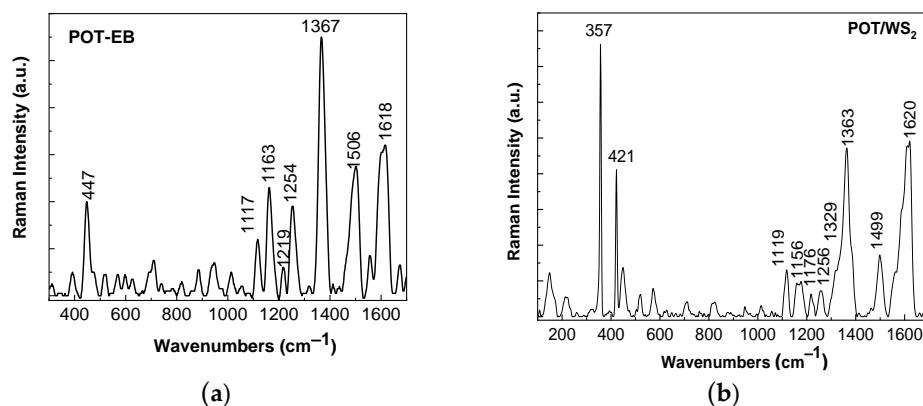

Figure 7. The Raman spectra of POT-EB (**a**) and the POT/WS$_2$ composite (**b**), with a TMD concentration of 20 wt.%, synthesized by ICP of OT.

The difference between vibrational modes E_{2g}^1 and A_{1g} of the POT/WS$_2$ composite is less than that obtained by the mechanical exfoliation of WS$_2$ NPs followed by ultrasonication in DMF. This fact indicates that the protocol for the preparation of WS$_2$ sheets, shown in the previous section, is most suitable for preparing composites based on POT and WS$_2$ sheets.

Information on potential interactions between constituents of the POT-EB/WS$_2$ composite, synthesized by ICP of OT in the presence of WS$_2$ NPs, is shown in Figure 8. Figure 8a shows the IR spectrum of POT-EB, which is characterized by IR bands located at 444, 816, 879, 1004, 1111, 1151, 1242, 1306, 1497, and 1601 cm^{-1}, attributed to vibrational modes of B deformation, out-of-plane deformation of the substituted B in the even position, deformation of triple-substituted B, deformation of B, deformation of the B + C-H bond in B, the C-H bond in-plane deformation of Q, stretching of the C-N bond in the B-N=Q structure, stretching of the C-N bond in Q, stretching of C-C + C-H + N-H bonds, and the structure of N=Q=N [32]. According to Figure 8b, the following vibrational changes are induced in POT by WS$_2$: (a) the IR bands are down-shifted from 1111, 1242, 1497, and 1601 cm^{-1} (Figure 8a) to 1105, 1213, 1490, and 1587 cm^{-1} (Figure 8b), accompanied by an up-shift in the IR band from 1306 cm^{-1} (Figure 8a) to 1313 cm^{-1} (Figure 8b); (b) a change in the absorbances ratios of the IR bands situated at (b$_1$) 1242–1213 cm^{-1} and 1497 cm^{-1} ($I_{1242\text{-}1213}/I_{1497}$) as well as (b$_1$) 1497 cm^{-1} and 1587–1601 cm^{-1} ($I_{1497}/I_{1587\text{-}1601}$) from 1.16 and 1.76 to 3.73 and 1, respectively. The IR bands that peaked at 3381 and 3730 cm^{-1} (Figure 8a) were assigned to

the N-H symmetric stretching [33] and free OH group [34] vibrational modes. In contrast to Figure 8a, the FTIR spectrum of the POT/WS$_2$ composite highlights the two IR bands situated at 3371 and 3729 cm^{-1}, the last one being accompanied by a new IR band at 3628 cm^{-1} assigned to the stretching OH vibrational mode [35]. An explanation for the OH vibrational mode must consider the generation of new hydrogen bonds between POT/WS$_2$ and H$_2$O molecules, according to Scheme 1.
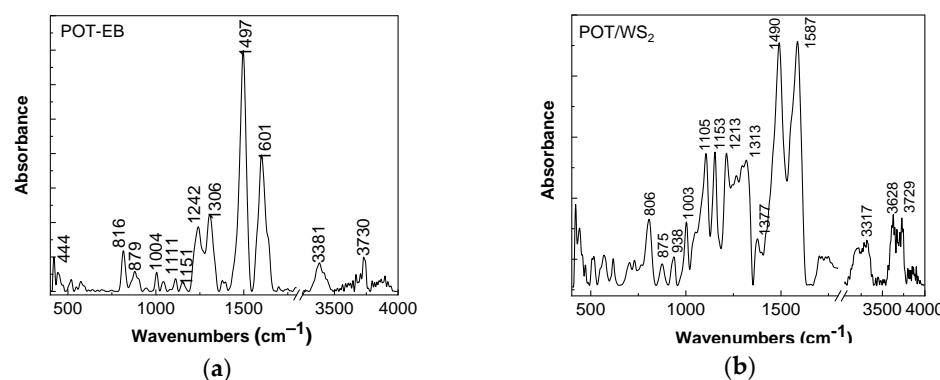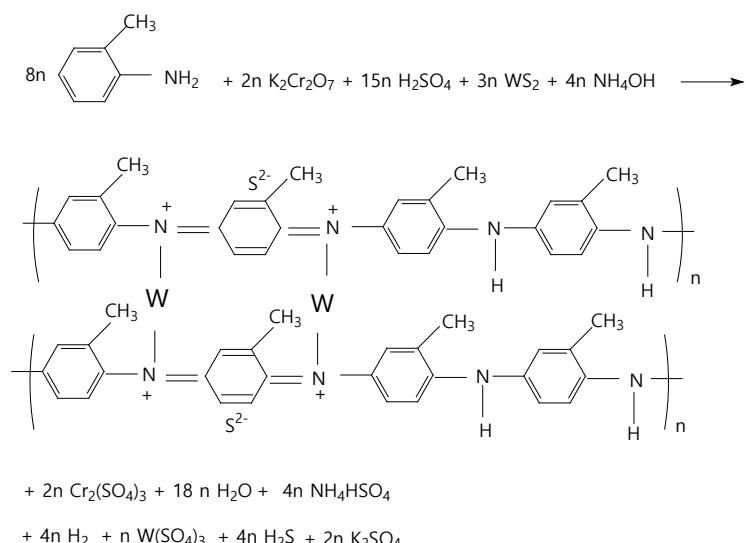
Figure 8. FTIR spectra of POT-EB (**a**) and POT/WS$_2$ composite (**b**), obtained by ICP of OT, with a WS$_2$ concentration in composite mass equal to 20 wt.%.

Scheme 1. Reaction of ICP of OT in the presence of WS$_2$ NPs.

In the case of the chemically synthesized POT/WS$_2$ composite, the following is observed by deconvolution: (a) In the XPS C1s spectrum, there are two bands of high intensity, with the maximum at 284.5 and 286.3 eV, which are accompanied by another five bands of lower intensity located at 287.3, 285.3, 284.8, 288.9, and 291 eV belonging to POT-EB (Figure 9a). The band from 291 eV corresponds to the π-π* transition of the aromatic ring of POT [36]. The bands that peak at 284.5, 284.8, 285.3 and 286.3 eV are assigned to bonds C=C (C hybridized sp^2), C-C/C-H, C-N/C=N, and C-O-H [37]. The bands that peak at 287.6 and 288.9 eV are assigned to the C=O and -COOR bonds existing as contaminants in the XPS installation. (b) In the XPS N1s spectrum, there are three bands located at 399.2, 399.9, and 401.4 eV (Figure 9b) that are assigned to bonds C-N=C [37], C-NH-C [37] and C-N$^+$ [38] of POT. (c) In the XPS W4f spectrum, three bands at 32.8, 34.9, and 35.9 eV (Figure 9c) are highlighted. The intense bands from 32.8 and 34.9 eV correspond to the doublet W 4f$^{7/2}$ and W 4f$^{5/2}$, which are separated by cca. 2.1 eV, the ratio of the areas of the two bands

being 4:3 [31]. The low-intensity band from 36.7 eV is associated with the $4f^{7/2}$ band of the tungsten sulfate adsorbed from the manufacturing process. (d) In the XPS S2p spectrum, four bands with maxima at 162.4, 163.6, 168.4, and 169.6 eV (Figure 9d) are remarked. The first two bands correspond to the $2p^{3/2}$ and $2p^{1/2}$ states, which are separated by cca. 1.18 eV, the ratio of the areas of the two bands being 2:1. The doublet from 162 to 163 eV represents 78% S from WS_2, while the doublet from 169 to 170 eV corresponds to 22% S from $W(SO_4)_3$. This fact indicates the presence of $W(SO_4)_3$ as a reaction byproduct in the WS_2 sample [31].
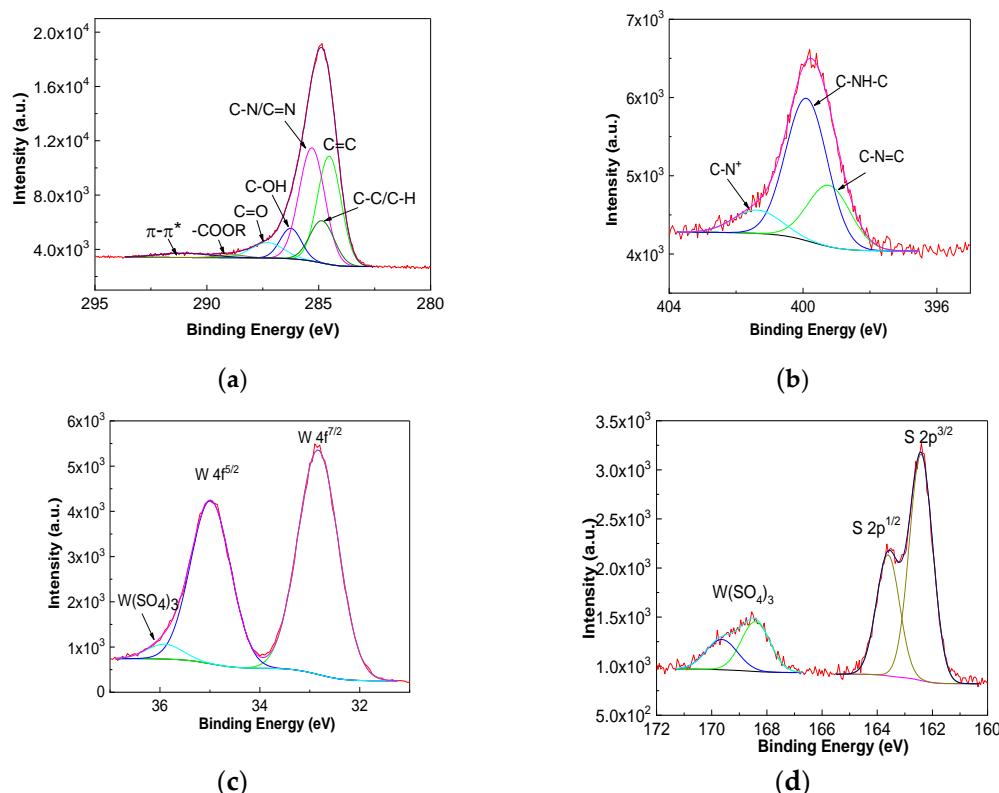

Figure 9. XPS C1s (**a**), W4f (**c**), S2p (**d**), and N1s (**b**) spectra of the POT/WS_2 composite with a WS_2 concentration in composite mass equal to 20 wt.%, synthesized by ICP of OT.

Considering the variations presented above, the total reaction of ICP of OT is shown in Scheme 1.

In our opinion, Scheme 1 explains the existence of the C-N=C, C-NH-C, and C-N$^+$ bonds in the POT-EB/WS_2 composites resulting from the ICP of OT in the presence of WS_2 NPs.

3.3. Electrochemical Synthesis of POT/WS_2 Composite and Its Optical Properties

Figure 10 shows the first 50 cyclic voltammograms recorded in the potential range (−200; +900) mV vs. Ag/AgCl, using a semi-aqueous solution of 0.1 M OT in 0.5 M H_2SO_4 (the volumetric ratio of DMF/H_2O was 1:1) and 0.5 mg/mL WS_2 sheets exfoliated according to the protocol reported in this work.
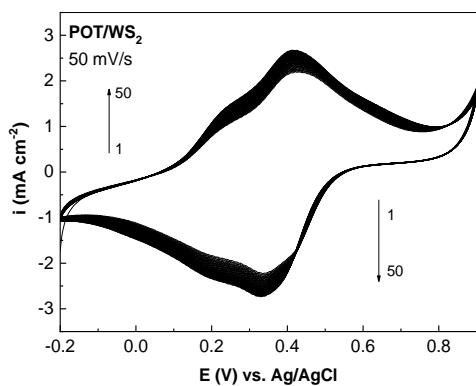
Figure 10. The first 50 cyclic voltammograms of ECP of OT in a solution of H_2SO_4 and WS_2 sheets, recorded at a potential scan rate of 50 mV/s.

The main changes in the cyclic voltammogram profile whilst increasing the cycle number recorded on the working electrode surface (Figure 10) can be quantified in the case of the following: (a) the first cyclic voltammogram, when the potential scanning takes place from (a_1) −200 to +900 mV vs. Ag/AgCl at the oxidation maximum with a potential of +418 mV, which is accompanied by another one with a potential of +246 mV, with the current densities of the two oxidation maxima at +418 and +246 mV equal to 2.12 mA/cm^2 and 1.06 mA/cm^2, respectively, and (a_2) +900 mV to −200 mV vs. Ag/AgCl, by a reduction maximum characterized by a potential equal to +334 mV, which is accompanied by another one with a potential of +200 mV; the two reduction maxima from +334 and +200 mV are characterized by current densities equal to 2.25 and 1.83 mA/cm^2, respectively; (b) the 50th cyclic voltammogram, when the potential scanning occurs from (b_1) −200 to +900 mV vs. Ag/AgCl, by an oxidation maximum with potential of +414 mV that is accompanied by another maximum with potential of +248 mV (the current densities of the two oxidation maxima at +414 and +248 mV are equal to 2.67 mA/cm^2 and 1.48 mA/cm^2), and (b_2) +900 mV to −200 mV vs. Ag/AgCl, where a reduction maximum characterized by a potential equal to +328 mV is observed, which is accompanied by another one with a potential of +198 mV; the two reduction maxima from +328 and +198 mV are characterized by current densities equal to 2.73 and 2.33 mA/cm^2, respectively. Regardless of the number of cyclic voltammograms recorded at the electrolyte/electrode interface, it is observed that two oxidation–reduction processes take place, which are evidenced by oxidation and reduction maxima with anodic and cathodic potentials located at (i) +418 mV and +334 mV as well as +246 mV and +200 mV in the first cyclic voltammogram, and (ii) +414 mV and +328 mV as well as +248 mV and +198 mV, respectively, in the 50th cyclic voltammogram. The above variations are accompanied by a progressive increase in the density of anodic and cathodic currents as the cyclic voltammogram number increases. The two oxidation–reduction processes are characterized by a potential difference of $\Delta E = E_a - E_c$, (where E_a and E_c are anodic and cathodic peak potential), equal to (i) 84 mV and 46 mV for the first cyclic voltammogram and (ii) 88 mV and 50 mV in the case of the 50th cyclic voltammogram. The ratio between the peak current densities of the anode to cathode (i_a/i_c) is equal to (i) 0.94 and 0.58 for the first cyclic voltammogram and (ii) 0.97 and 0.63 in the case of the 50th cyclic voltammogram. Analyzing the above results, it is noticed that there are oxidation–reduction processes for which ΔE differs by 56.5 mV/n, where n is the number of electrons involved in the oxidation–reduction process, and/or the ratio of anodic to cathodic current densities (i_a/i_c) differs from one, facts which allows us to conclude that the ECP of OT onto a Pt electrode in the presence of WS_2 sheets is an irreversible process. After 50 cyclic voltammograms, a dark green film is generated on the Pt electrode surface as a consequence of the generation of the POT-ES/WS_2 composite. To confirm the

formation of this composite, Figure 11 shows the Raman spectrum of the POT-ES/WS$_2$ composite synthesized electrochemically on the Pt electrode surface, after recording the 50th cyclic voltammogram.
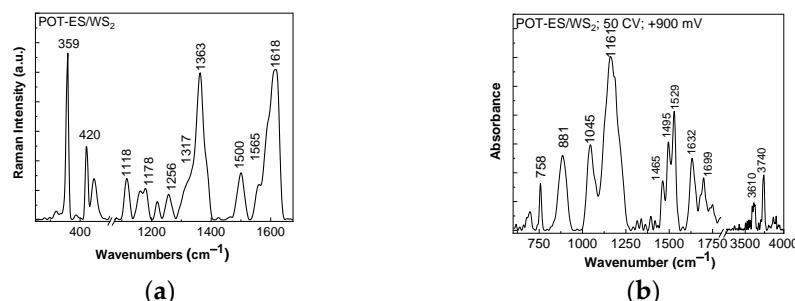

Figure 11. Raman spectrum (**a**) and FTIR spectrum (**b**) of the POT-ES/WS$_2$ composite synthesized by ECP on the Pt electrode surface after recording 50 cyclic voltammograms.

According to Figure 11a, the Raman spectrum of the POT-ES/WS$_2$ composite is characterized by Raman lines located at (a) 359 and 420 cm^{-1}, coming from WS$_2$ sheets, being related to vibrational modes E$_{2g}^1$ and A$_{1g}$ [24], and (b) 1118, 1178, 1256, 1317, 1363, 1500, and 1618 cm^{-1}, belonging to POT-ES [31,32]. The FTIR spectrum of the electrochemically synthesized POT-ES/WS$_2$ composite after recording 50 cyclic voltammograms in the range (−200; +900) mV (Figure 11b) is characterized by IR bands situated at 758, 881, 1045, 1161, 1465 −1495, 1529, and 1632 cm^{-1}. According to Ref. [39], the FTIR spectrum of POT-ES is characterized by IR bands localized at 754, 889, 1045, 1145–1185, 1481–1489, and 1610 cm^{-1} that are attributed to the following vibrational modes: B deformation, Q deformation, out-of-plane deformation of triple-substituted B, (B)-NH$^+$=(Q), N-B-N, and N=Q. The differences concerning the wavenumbers of IR bands associated with the vibrational modes of B–NH$^+$=Q and N=Q can be explained by steric hindrance effects due to the covalent coordination bonds established between W atoms in WS$_2$ and amine groups of POT-ES. According to Figure 11b, the IR bands assigned to the stretching OH and free OH group vibrational modes peaked at 3610 and 3740 cm^{-1}. A careful analysis of Figures 8b and 11b highlights that the ratio between the absorbance of the OH stretching vibrational mode and free OH groups is equal to 1 and 0.5, respectively. The low absorbance of the IR band assigned to OH bond vibration indicates a small proportion of hydrogen bonds and a low degree of connectivity of molecules through hydrogen bonds for the samples resulting from ECP. More information about the bonds existing in the electrochemically synthesized POT-ES/WS$_2$ composite is presented in the following by XPS. Figure 12 illustrates the XPS spectra of the electrochemically synthesized POT/WS$_2$ composite, for which the deconvolution of (a) the XPS C1s spectrum highlights a band of high intensity at 284.3 eV and another three bands of lower intensity situated at 285.1, 285.7, and 286.8 eV belonging to POT-ES (Figure 12a). The bands from 284.3, 285.1, 285.7, and 286.8 eV have been assigned to the bonds C=C (C hybridized sp^2), C-C/C-H, C-N/C=N, and C-O-H [34]. (b) The XPS N1s spectrum highlights three bands located at 399.2, 399.9, and 401.4 eV (Figure 12b), which have been assigned to bonds C-N=C [37], C-NH-C [37], and C-N$^+$ [38]. (c) The XPS W4f spectrum highlights two bands at 32.6 and 34.7 eV (Figure 12c), corresponding to the doublet W 4f$^{7/2}$ and W 4f$^{5/2}$, the two bands being separated with cca. 2.1 eV, the ratio of areas being 4:3. (d) The XPS S2p spectrum leads to four bands with maxima at 162.1, 163.3, 168, and 169.2 eV (Figure 12d).
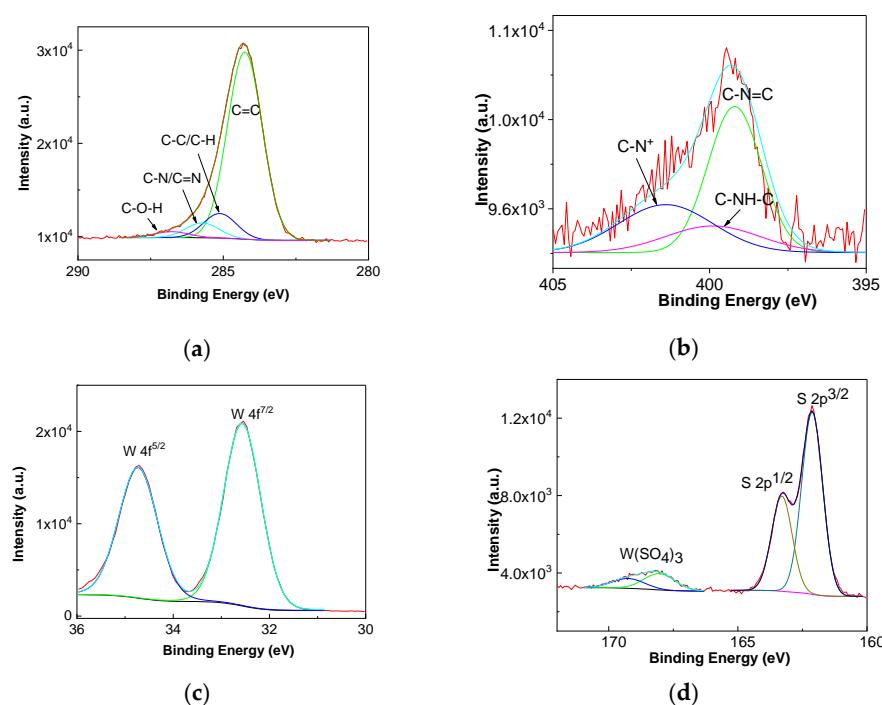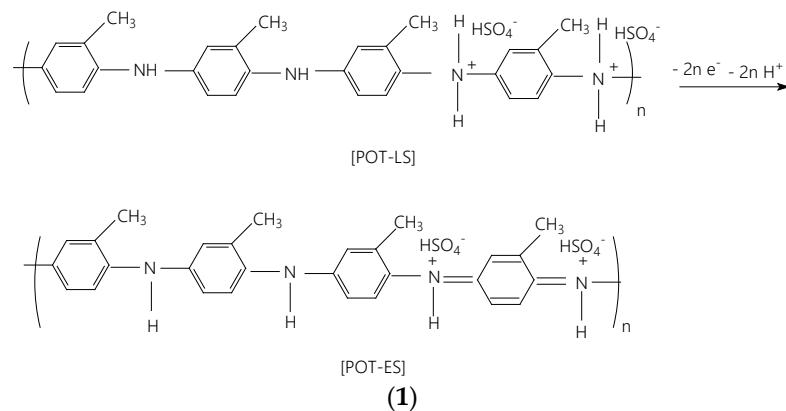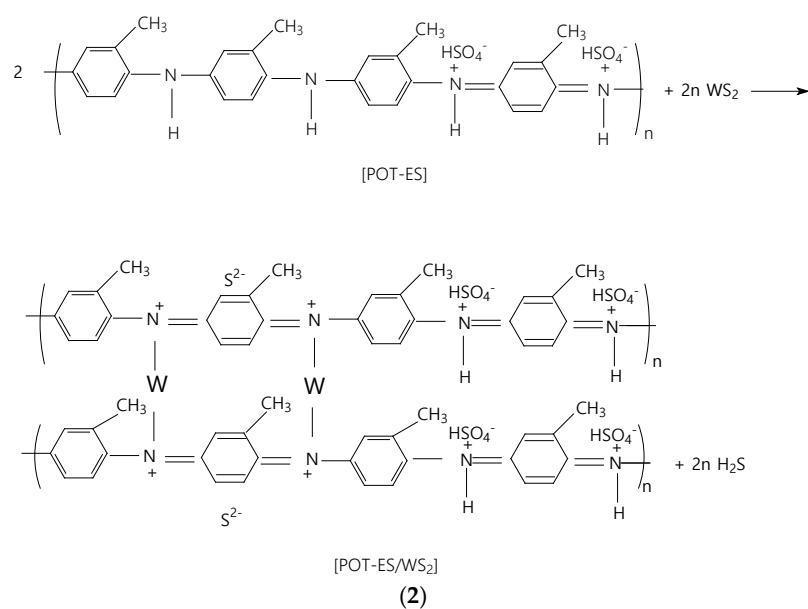
Figure 12. XPS spectra C1s (**a**), N1s (**b**), W4f (**c**), and S2p (**d**) of the POT-ES/WS$_2$ composite synthesized by the electrochemical method.

The first two bands correspond to the 2p$^{3/2}$ and 2p$^{1/2}$ states, which are separated by cca. 1.18 eV, the ratio of the areas of the two bands being 2:1. The doublet from 162 to 163 eV represents S from WS$_2$, while the doublet from 168 to 169 eV corresponds to S derived from W(SO$_4$)$_3$. This fact indicates that the polymerization reaction leads to a byproduct of the type W(SO$_4$)$_3$. All these changes clearly prove the generation of POT-ES/WS$_2$ composites by the ECP method. The chemical mechanism that can explain the electrochemical generation of the POT/WS$_2$ composite on the Pt electrode surface takes into account (i) the oxidation reaction of OT when a cation radical of OT is produced, which is unstable and consequently reacts with itself, forming the dimer of OT; (ii) further, macromolecular chain growth involves a propagation reaction when the dimer is successively transformed into a trimer, oligomer, and polymer, with POT thus obtained being in a leucoemeraldine base (LB) state, which reacts with H$_2$SO$_4$ and leads to POT in leucoemeraldine salt (LS). According to Scheme 2, the oxidation reaction of POT-LS leads to the generation of POT- ES, which chemically interacts with WS$_2$, resulting in the POT-ES/WS$_2$ composite.

Scheme 2. *Cont.*

Scheme 2. The mechanism of EC synthesis of the POT/WS$_2$ composite: (**1**) oxidation reaction of POT-LS with the generation of POT-ES; (**2**) chemical interaction of POT-ES with WS$_2$.

3.4. Electrochemical Properties of the POT/WS$_2$ Composites as Promising EAM in Supercapacitor Cells

Figure 13 shows cyclic voltammograms of the POT-EB/WS$_2$ and POT-ES/WS$_2$ composites, prepared by SSI and ICP, respectively, when a Nafion membrane that interacted with H$_2$SO$_4$ 1M was used as an electrolyte. A careful analysis of Figure 13a,b highlights higher values of the voltametric output currents of the POT-EB/WS$_2$ and POT-ES/WS$_2$ composites than of POT-EB and POT-ES. These results allow us to anticipate that the high capacitance value of the POT-EB/WS$_2$ and POT-ES/WS$_2$ composites would be obtained.
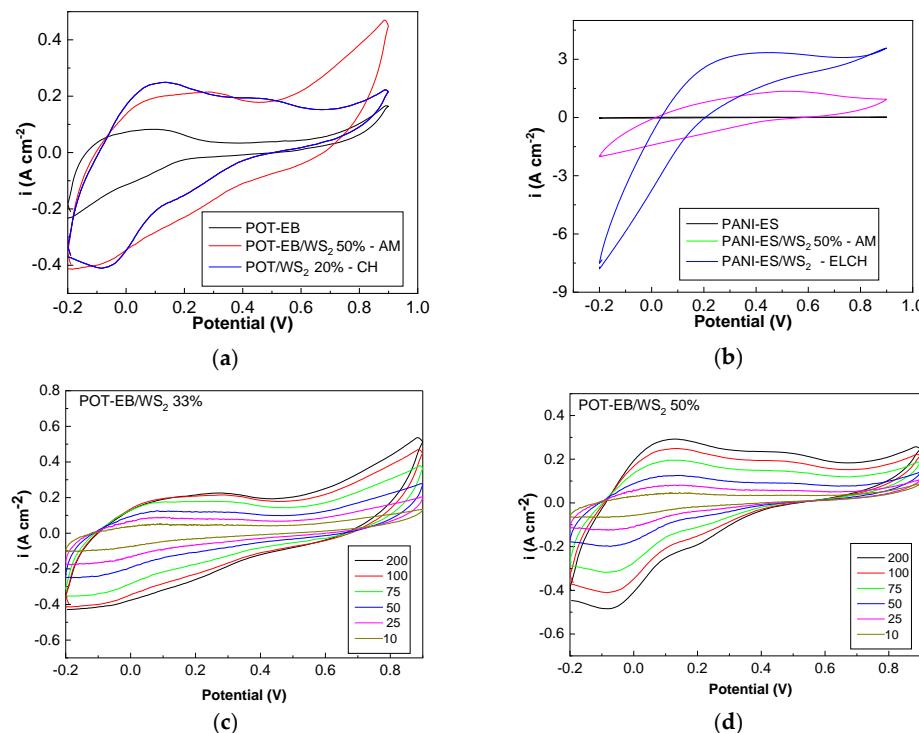
Figure 13. *Cont*.
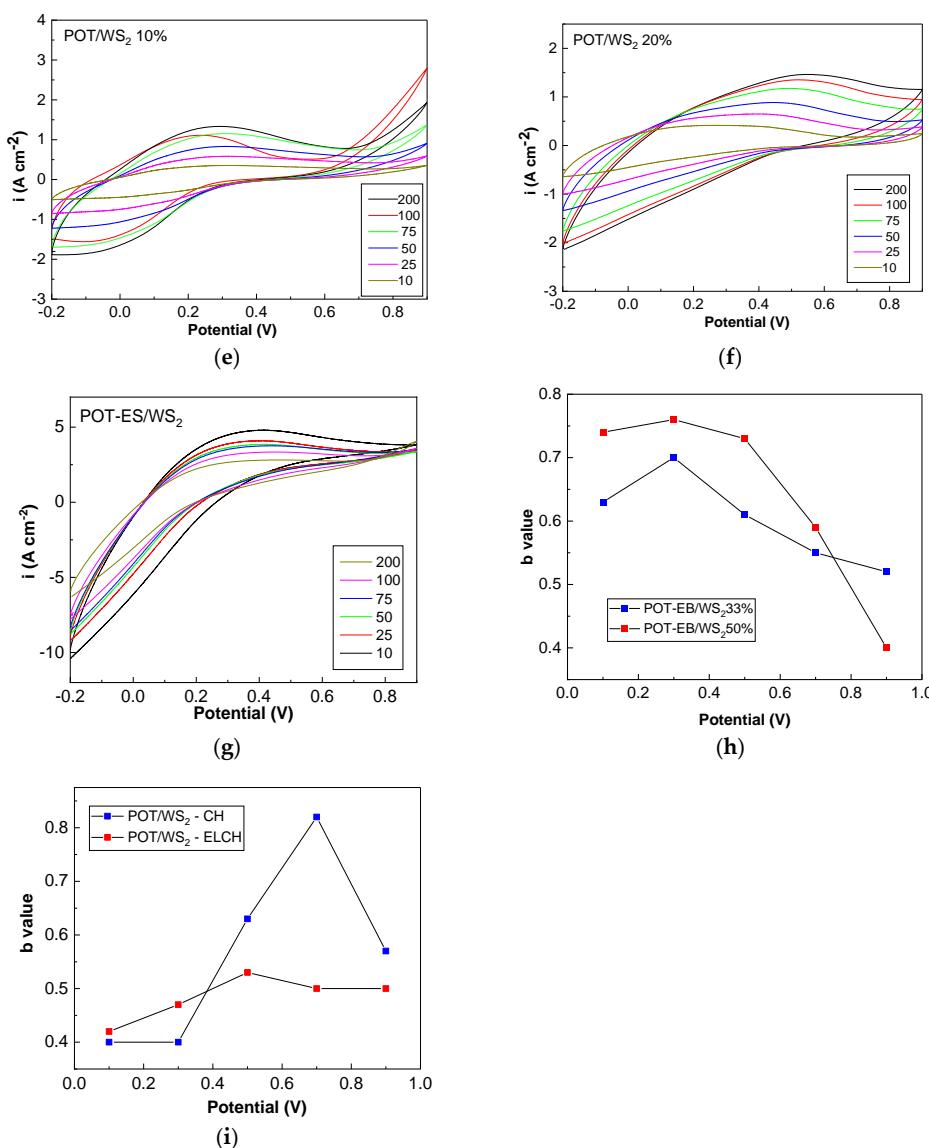
Figure 13. The 5th cyclic voltammogram of (**a**) POT-EB (black curve), the POT-EB/WS$_2$ composite synthesized by chemical polymerization (with a WS$_2$ concentration in composite mass equal to 50 wt.%, red curve), and the POT-EB/WS$_2$ composite resulting from SSI of the two compounds when the WS$_2$ concentration in the composite mass is equal to 20 wt.% (blue curve) and the scan rate is 100 mV s^{-1}; (**b**) POT-ES (black curve), the electrochemically synthesized POT-ES/WS$_2$ composite (blue curve), and the POT-ES/WS$_2$ composite obtained by SSI when the WS$_2$ concentration in the composite mass is 20 wt.% (red curve), when the scan rate is 100 mV s^{-1}; the POT-EB/WS$_2$ composites with a WS$_2$ concentration equal to 33 wt.% (**c**) and 50 wt.% (**d**); the POT/WS$_2$ composites, synthesized by ICP, when the WS$_2$ concentration in the composite mass is equal to 10 wt.% (**e**) and 20 wt.% (**f**); and the POT-ES/WS$_2$ composite synthesized by the ECP method (**g**). Black, red, green, blue, magenta, and dark yellow curves in (**c**–**g**) show the cyclic voltammograms recorded at 200, 100, 75, 50, 25, and 10 mV s^{-1}. (**h**) The variation in the b value with voltage in the case of the POT-EB/WS$_2$ composites synthesized by SSI of POT-EB with WS$_2$ nanoparticles, when the WS$_2$ concentration is equal to 33 wt.% (blue square) and 50 wt.% (red square); (**i**) the dependence of the b value on voltage for the POT/WS$_2$ composites with the WS$_2$ concentration of 20 wt.%, synthesized by chemical polymerization of OT assisted by WS$_2$ (blue square), and the POT-ES/WS$_2$ composites synthesized by the ECP method (red square).

Using the equation i(V) = a x v^b, where I, v, a, and b correspond to current density (A cm^{-2}), potential scan rate (mV s^{-1}), and the two constants, we calculate the contribution of the capacitive process due to the double-layer charge at the electrolyte/electrode interface

and diffusion processes [40]. According to Ref. [40], depending on the value of the b constant, (a) a redox reaction at the electrode surface and the charge/discharge processes of the electric double-layer capacitors (EDLCs) occur when b = 1; (b) a pseudocapacitive process takes place when 0.8 < b < 1; and (c) a behavior of the type battery is invoked when 0.5 < b < 0.8. With all these in mind, from plot log(i) to log(v), we have determined that all samples show battery behavior. The contribution of the surface capacitive and diffusion-controlled intercalation (DCI) processes in cyclic voltammograms can be assessed using the protocol published in Ref. [31]. Thus, using the equation $i(V) = k_1 v + k_2 v^{1/2}$, where $i(V)$, $k_1 v$, and $k_2 v^{1/2}$ are current density for a fixed potential, the weight of the capacitive effect, and the intercalation process, respectively, and applying a linear fit in the case of the plot $i(V)/v^{1/2}$ vs. $v^{1/2}$, the values of k_1 and k_2 were determined. The contribution of the two processes is shown in Figures 14 and 15.


(a)

(b)

(c)

(d)

(e)
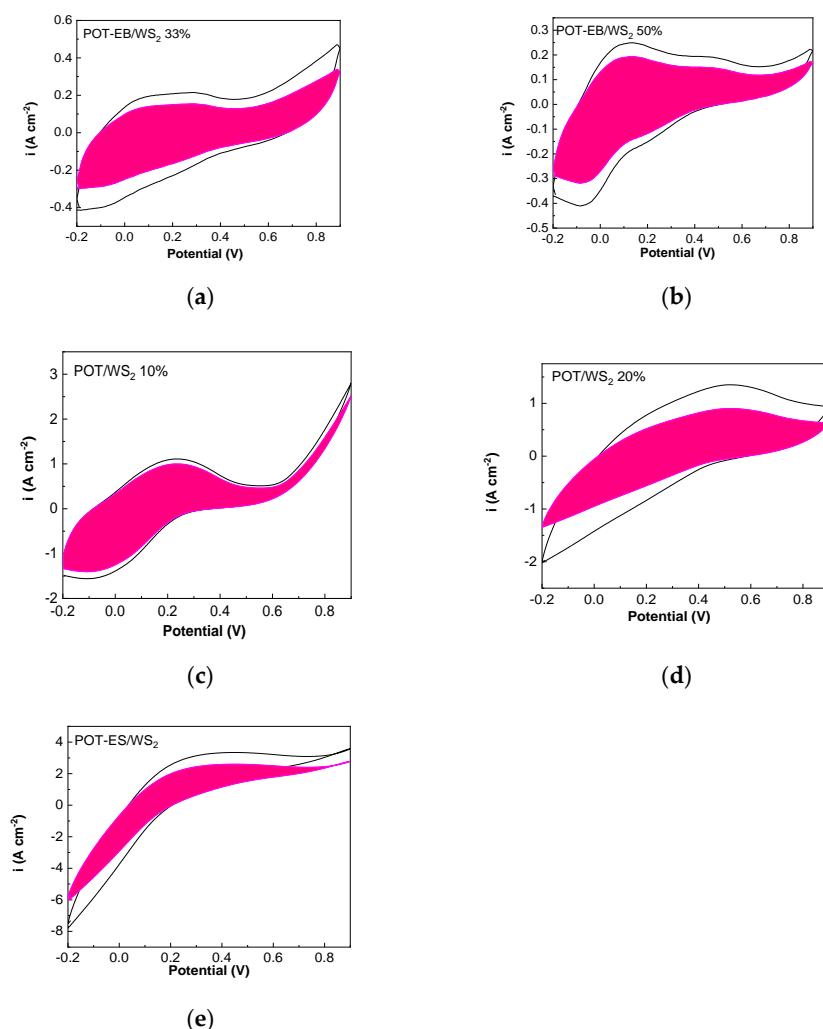
Figure 14. Deconvoluted intercalation (pink area) and capacitance (white area) processes of the POT-EB/WS$_2$ composites with WS$_2$ concentrations of 33 wt.% (**a**) and 50 wt.% (**b**); the POT/WS$_2$ composite with a WS$_2$ concentration in the composite mass equal to 10 wt.% (**c**) and 20 wt.% (**d**), prepared by the ICP method; and the POT-ES/WS$_2$ composite obtained by the ECP method (**e**), when the cyclic voltammograms were recorded at a scan rate of 100 mV s^{-1}.

According to Figures 14 and 15, all samples show a significant contribution given the diffusion-controlled intercalation process, which is accompanied by a capacitive process. Scheme 3 shows the reactions at the electrolyte/electrode interface when the electrodes contain the composites prepared by ICP and ECP.
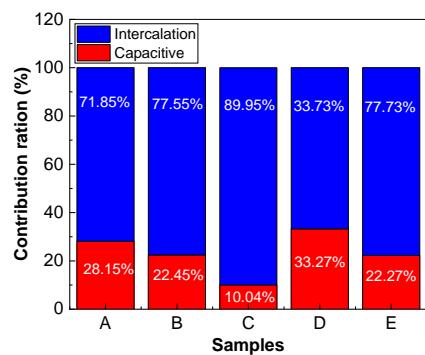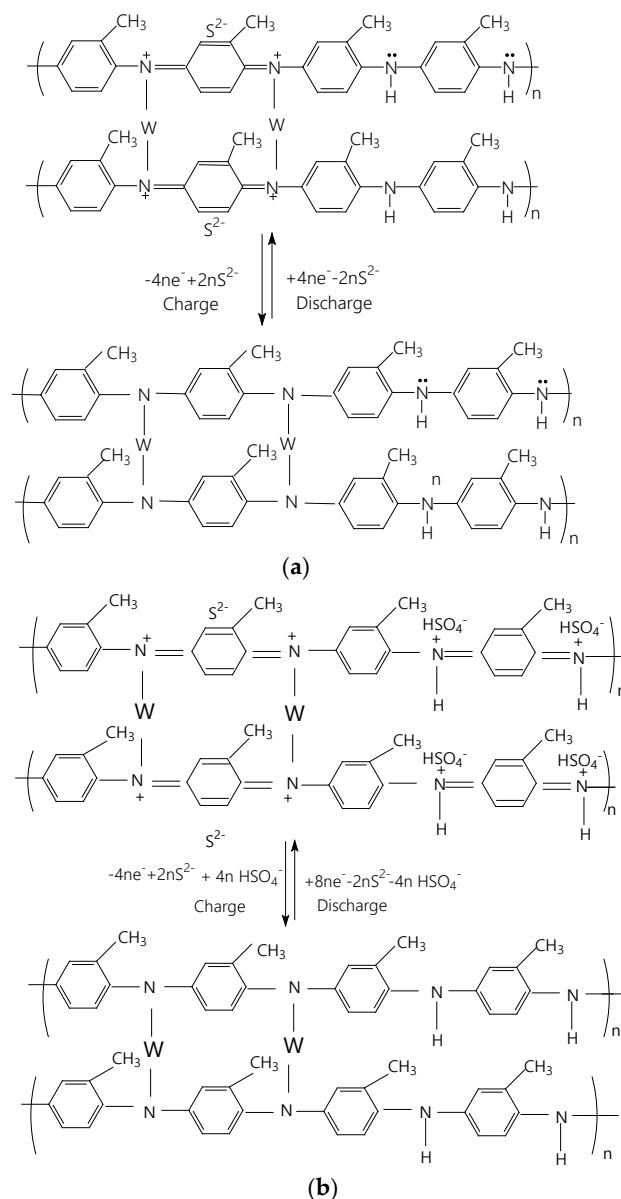
Figure 15. Contribution ratio between capacitive and diffusion processes of POT-EB/WS$_2$ composites with WS$_2$ concentrations of 33 wt.% (sample A) and 50 wt.% (sample B), the POT/WS$_2$ composites synthesized by the ICP method (WS$_2$ concentration in composite mass is 10 wt.% (sample C) and 20 wt.% (sample D)), and the POT-ES/WS$_2$ composite synthesized by the ECP method (sample E).

(**a**)

(**b**)

Scheme 3. The reactions at the electrolyte/electrode interface of the electrodes containing the POT/WS$_2$ composites synthesized by ICP (**a**) and the POT-ES/WS$_2$ composite synthesized by ECP (**b**).

Figure 16 shows the variation in capacitance vs. scan rate of the electrodes prepared in this study.
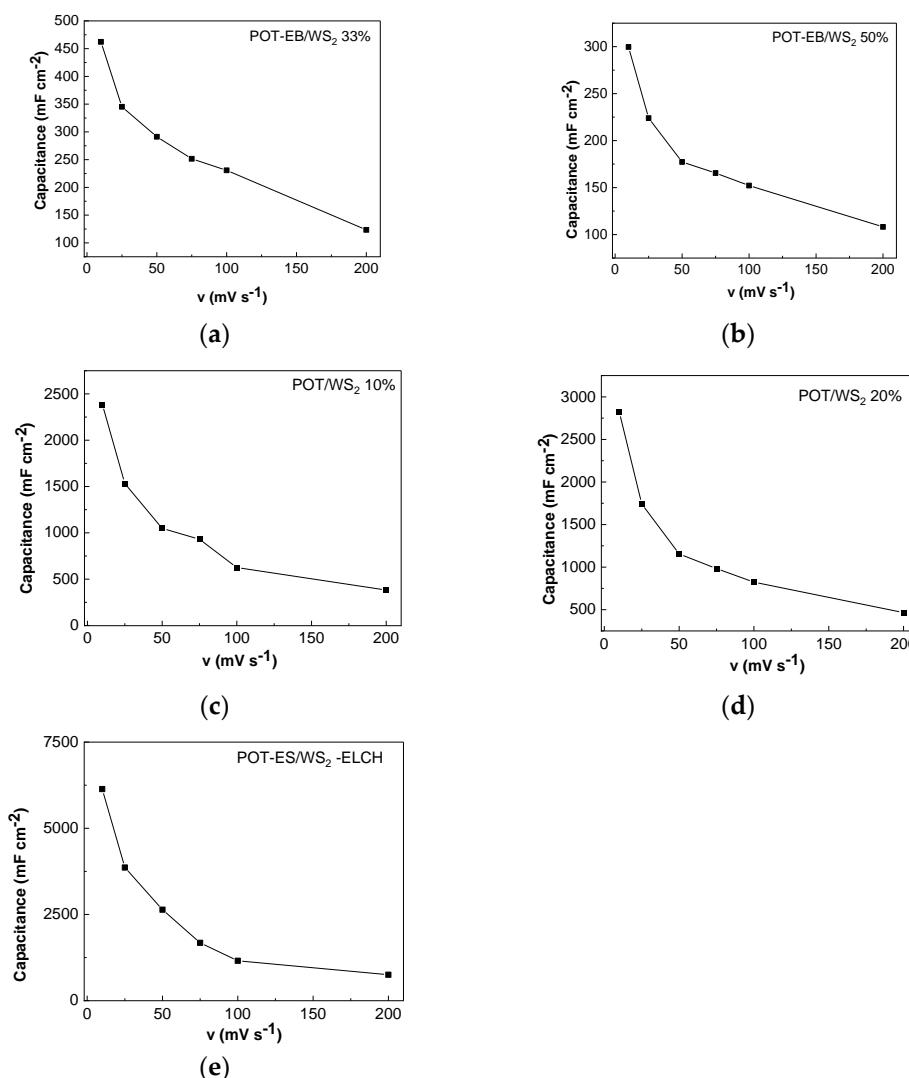

Figure 16. The dependence of capacitance vs. potential scan rate of electrodes based on the POT-EB/WS$_2$ composites resulting from SSI with WS$_2$ concentrations equal to 33 wt.% (**a**) and 50 wt.% (**b**); the POT-EB/WS$_2$ composites synthesized by ICP with WS$_2$ concentrations equal to 10 wt.% (**c**) and 20 wt.% (**d**); and the POT-ES/WS$_2$ composite synthesized by the ECP method (**e**).

At a scan rate of 10 mV s^{-1}, the capacitance of the SCs with composites prepared by ICP and ECP was equal to 2.82 and 12.5 F cm^{-2}. A decrease in capacitance when increasing the potential scan rate from 10 to 200 mV/s takes place for (i) the POT-EB/WS$_2$ composites resulting from the SSI method, which have WS$_2$ concentrations equal to 33 wt.% and 50 wt.%, from 462.18 and 299.68 mF cm^{-2} to 123.52 and 108.16 mF cm^{-2}; (ii) the POT/WS$_2$ composites, synthesized by the ICP method, when the TMD concentration in the composite mass is 10 wt.% and 20 wt.%, from 2386.2 and 2820.71 mF cm^{-2} to 382.69 and 465.76 mF cm^{-2}; and (iii) the POT-ES/WS$_2$ composite synthesized by the ECP method from 6136.75 to 751.6 mF cm^{-2}. Figure 17 shows the variation in the capacitance of the SCs with the cyclic voltammogram numbers, in the case of electrodes based on (i) the POT-EB/WS$_2$ composite resulting from the interaction of the two constituents when the WS$_2$ concentration is 50 wt.%; (ii) the POT/WS$_2$ composite, synthesized by the chemical polymerization of OT, when the WS$_2$ concentration is 20 wt.%; and (iii) the electrochemical synthesized POT-ES/WS$_2$ composite.

(a)

(b)

(c)
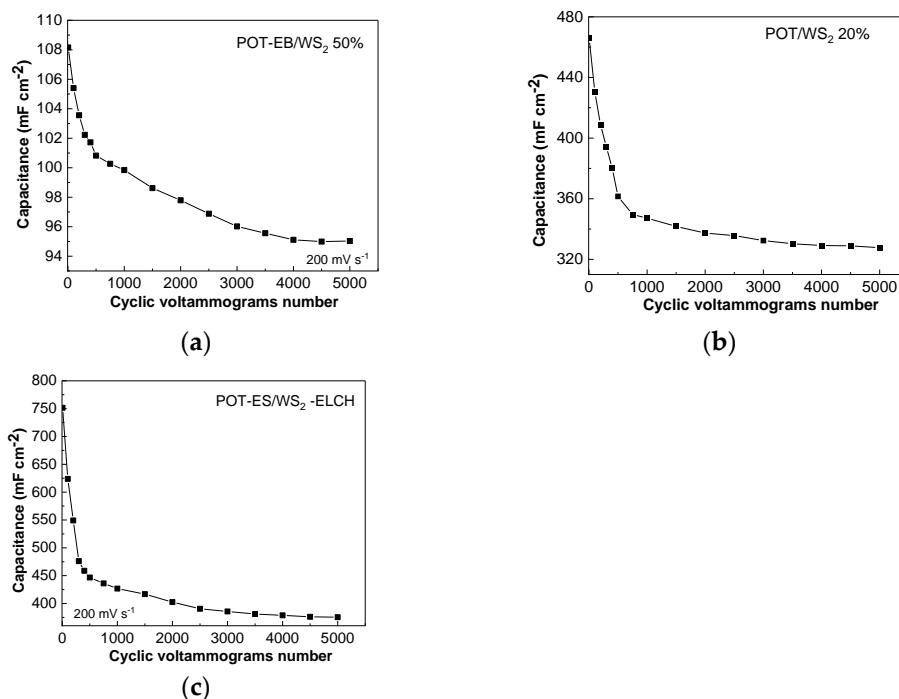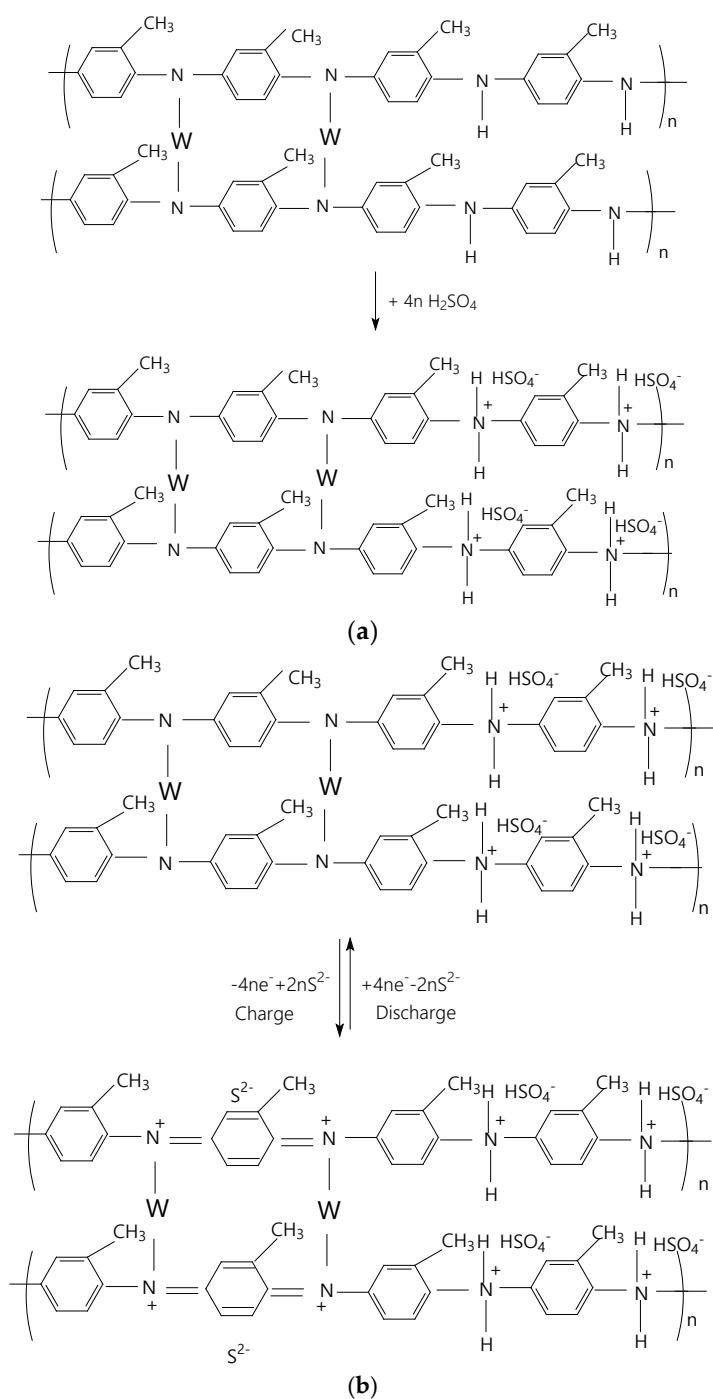
Figure 17. The variation in capacitance vs. number of cyclic voltammograms recorded at 200 mV s^{-1} of electrodes based on (**a**) the POT-EB/WS$_2$ composite prepared by the SSI method, when the WS$_2$ concentration in composite mass was 50 wt.%; (**b**) the POT/WS$_2$ composite, synthesized by ICP (the WS$_2$ concentration in the composite mass was 20 wt.%); and (**c**) the POT-ES/WS$_2$ composite, synthesized by the ECP method.

According to Figure 17, an important decrease in the capacitance takes place in the first 750 cyclic voltammograms for the POT/WS$_2$ composites prepared by the three synthesis methods. This behavior should be explained by considering various expansions and contractions of the volume of the electrode as a consequence of the expulsion and insertion of ions during discharge and charge processes, as shown in Schemes 3 and 4.

Scheme 3 highlights, based on Equations (1) and (2), that during the discharge half-cycle of the first cyclic voltammogram, the HSO$_4^-$ and S^{2-} ions leave the POT-ES/WS$_2$ composites, with the macromolecular compounds having an LB structure. In the charge half-cycle of the first cyclic voltammogram, both the HSO$_4^-$ and S^{2-} ions will inserted into the composite matrix. Scheme 4 shows the chemical reaction that can occur after the discharge half-cycle of the first cyclic voltammogram considering the H$^+$ and HSO$_4^-$ ions of the Nafion membrane treated with H$_2$SO$_4$, which interact with the amine groups according to Equation (1) when POT-LB/WS$_2$ is transformed into POT-LS/WS$_2$. This fact indicates that, in the following cyclic voltammograms, the charge/discharge processes take place according to Equation (2). Increasing the number of cyclic voltammograms will induce more and more amine groups to react with H$_2$SO$_4$ according to Equation (1), which, in our opinion, may explain the decrease in SC capacitance in the first 750 cyclic voltammograms and the degradation of EAM. After recording 5000 cyclic voltammograms, the values of the capacitance of the supercapacitor cells with electrodes based on the POT/WS$_2$ composites obtained by SSI, ICP, and ECP are equal to 95.03 (Figure 17a), 327.71 (Figure 17b), and 375.33 mF/cm^2 (Figure 17c).

(a)

+ 4n H$_2$SO$_4$

(b)

-4ne$^-$+2nS^{2-} Charge

+4ne$^-$-2nS^{2-} Discharge

Scheme 4. Reactions during discharge and charge processes in SC cell containing POT-ES/WS$_2$ composite as EAM: (**a**) the reaction of the POT-LB/WS$_2$ composite with H$_2$SO$_4$ (Equation (1)) and (**b**) charge/discharge processes of the POT-LS/WS$_2$ composite (Equation (2)).

The differences between the capacitance values of supercapacitors containing the PANI/WS$_2$ and POT/WS$_2$ composites, prepared in different ways and using various synthesis methods or suppliers for WS$_2$ particles, are summarized in Table 1 [41–46]. According to Table 1, the capacitance value depends on the shape of the WS$_2$ particles, the synthesis method of the composites used as active materials in the SC cells, the type of electrolyte, and the applied current densities. Table 1 further presents the performance of SCs with PANI/MnO$_2$ and polybenzidine/MnO$_2$ composites as EAMs. The comparison between SCs with composites of the type PANI/WS$_2$ [42,44] and γ-MnO$_2$/PANI [45] as the EAM indicates that the former shows higher values of capacitance. In the case of SCs based

on POT/WS$_2$ composites, which were prepared by ICP and ECP, higher capacitance values of 2.82 and 12.5 F cm^{-2} at a potential scan rate of 10 mV s^{-1} are reported in comparison with the SC containing polybenzidine/MnO$_2$ as the EAM [46]. In this stage of our investigations, to optimize the SCs developed in this work, we plan to test SC cells by preparing new POT/WS$_2$ composites, in which WS$_2$ sheets will be replaced by WS$_2$ rods. Considering the work reported by Zhang et al [16], which demonstrated that by doping PANI with HClO$_4$ and p-toluenesulfonic acid (p-TSA), respectively, higher energy density values can be obtained only in the former case, another parameter to be considered for improving the performance of SCs containing POT/WS$_2$ is co-doping with a suitable dopant agent such as HClO$_4$. An electrolyte often used in the SC field containing sulfides [47,48] or MnO$_2$ [44] is KOH, which will be considered by us in future studies.

Table 1. The performance of SCs based on PANI/WS$_2$, POT/WS$_2$, PANI/MnO$_2$, and polybenzidine/MnO$_2$ composites.

EAMs; Inorganic Particle Synthesis Method or Supplier	Synthesis Method of Composite	Electrolyte	Current Density or Potential Scan Rate	Capacitance	Ref.
PANI/WS$_2$/C; Merck	ICP	1M Na$_2$SO$_4$	10 mVs^{-1}	464 F g^{-1}	[41]
PANI nanofibers/WS$_2$; Sigma Aldrich	Electrodeposition by CV	1M Na$_2$SO$_4$	1Ag^{-1}; 5000 V s^{-1}	72.27 F g^{-1}; 331 mF cm^{-2}	[41]
PANI/WS$_2$; hydrothermal	ICP	1M H$_2$SO$_4$	1Ag^{-1}	560 F g^{-1}	[42]
PANI/WS$_2$; mechano-chemically assisted NaCl	Mechano-chemical reaction	1M H$_2$SO$_4$	1Ag^{-1}	580 F g^{-1}	[43]
POT/WS$_2$; ball milling	SSI	1M H$_2$SO$_4$	50 mV s^{-1}	177 mF cm^{-2}	This work
POT/WS$_2$; ball milling	ICP	1M H$_2$SO$_4$	50 mV s^{-1}	1.15 F cm^{-2}	This work
POT/WS$_2$; ball milling	ECP by CV	1M H$_2$SO$_4$	50 mV s^{-1}	2.64 F cm^{-2}	This work
MnO$_2$ Nanorods@PANI; hydrothermal	ICP	1M KOH	50 mVs^{-1}	259 F g^{-1}	[44]
γ-MnO$_2$/PANI; from precursor of KMnO$_4$	ICP	0.5M H$_2$SO$_4$	0.5 A g^{-1}	493 F g^{-1}	[45]
Polybenzidine/MnO$_2$	Chemical interaction	1M H$_2$SO$_4$	0.5 mAcm^{-2}	950 mF cm^{-2}	[46]
POT/WS$_2$; ball milling	ICP	1M H$_2$SO$_4$	10 mVs^{-1}	2.82 F cm^{-2}	This work
POT/WS$_2$; ball milling	ECP by CV	1M H$_2$SO$_4$	10 mVs^{-1}	12.5 F cm^{-2}	This work

4. Conclusions

The synthesis methods of the POT/WS$_2$ composites, their optical and structural properties, and their applications in the symmetrical SC field were reported. Using SEM, XRD, FTIR spectroscopy, Raman scattering, XPS, UV-VIS spectroscopy, and CV, the following conclusions are highlighted:

(i) Mechanical exfoliation by grinding WS$_2$ NPs using a ball mill followed by exfoliation in DMF allows the transformation of nanoparticles of WS$_2$ in sheets and induces a diminution in the intensity of the crystalline plane (002), a change in the distance between the Raman lines related to vibrational modes E$_{2g}^1$ and A$_{1g}$, and the presence of three bands situated at 632, 530, and 454 nm in the UV-VIS spectrum.

(ii) SSI of POT-EB with WS$_2$ induces an exfoliation of the WS$_2$ NPs.

(iii) ICP of OT in the presence of WS$_2$ sheets induces the formation of covalent coordination bonds between the imine groups of EB and the transition metal W, when a POT/WS$_2$ composite is created, simultaneously with the generation of a byproduct such as tungsten sulfate.

(iv) ECP of OT in the presence of WS$_2$ sheets involves oxidation and reduction reactions at the electrolyte/electrode interface that have an irreversible character as a result

of the generation of the POT-ES/WS$_2$ composite when the formation of covalent coordination bonds between imine groups of POT and W atoms of TMD takes place.

(v) The electrochemical processes at the electrode/electrolyte interface in symmetrical SCs show a significant contribution given the performance of a diffusion-controlled intercalation process and an additional capacitive-type process; the best values of capacitance of the SCs with EAMs of the composites prepared by ICP and ECP were reported at 10 mV s^{-1}, these being equal to 2.82 and 12.5 F cm^{-2}; the increase in the scan rate at 200 mV s^{-1} led to values of capacitance equal to 123.5, 465.76, and 751.6 mF cm^{-2}, respectively, for the POT/WS$_2$ composites prepared by SSI, ICP, and ECP. After recording 5000 cyclic voltammograms at 200 mV s^{-1}, a decrease in the capacitance of the three SCs to 95.03, 327.71, and 375.33 mF cm^{-2} was reported.

Author Contributions: Conceptualization, M.B.; methodology, M.B. and A.U.; validation, M.B.; investigation, T.B., I.S., A.A., C.S.F., M.C., M.P., A.U., A.L., P.P., A.G., C.N., E.M., M.D., R.C. and M.B.; writing—original draft preparation, M.B.; writing—review and editing, M.B., A.U., A.L., C.N. and P.P.; visualization, T.B., I.S., A.A., C.S.F., M.C., M.P., A.U., A.L., P.P., A.G., C.N., E.M., M.D. and R.C.; supervision, M.B. All authors have read and agreed to the published version of the manuscript.

Data Availability Statement: The original contributions presented in this study are included in the article. Further inquiries can be directed to the corresponding author.

Conflicts of Interest: The authors declare no conflicts of interest.

Abbreviations

The following abbreviations are used in this manuscript:

POT	Poly(o-toluidine)
OT	O-toluidine
NPs	Nanoparticles
XRD	X-ray diffraction
XPS	X-ray photoelectron spectroscopy
UV-VIS	Ultraviolet–visible
FTIR	Fourier transform infrared
LS	Leucoemeraldine salt
ES	Emeraldine salt
EB	Emeraldine base
TMDs	Transition metal dichalcogenides
PANI	Polyaniline
SEM	Scanning electron microscopy
DMF	N,N′-dimethyl formamide
PVDF	Poly(vinylidene fluoride)
DBP	Dibutyl phthalate
CV	Cyclic voltammetry
SSI	Solid-state interaction
ICP	In situ chemical polymerization
ECP	Electrochemical polymerization
SCs	Supercapacitors
SA	Surface area
EAMs	Electrode active materials
B	Benzene ring
Q	Quinoid ring

DCI	Diffusion-controlled intercalation
EC	Electrochemical
λ_{exc}	Excitation wavelength

References

1. Shahabuddin, S.; Mehmood, S.; Ahmad, I.; Sridewi, N. Synthesis and Characterization of 2D-WS2 Incorporated Polyaniline Nanocomposites as Photo Catalyst for Methylene Blue Degradation. *Nanomaterials* **2022**, *12*, 2090. [CrossRef] [PubMed]

2. Parangusan, H.; Bhadra, J.; Al-Qudah, R.A.; Elhadrami, E.C.; Al-Thani, N.J. Comparative Study on Gas-Sensing Properties of 2D (MoS_2, WS_2)/PANI Nanocosmposites-Based Sensor. *Nanomaterials* **2022**, *12*, 4423. [CrossRef] [PubMed]

3. Iqbal, M.; Saykar, N.G.; Alegaonkar, P.S.; Mahapatra, S.K. Synergistically modified WS_2@PANI binary nanocomposite-based all-solid-state symmetric supercapacitor with high energy density. *New J. Chem.* **2022**, *46*, 7043–7054. [CrossRef]

4. De Adhikari, A.; Shauloff, N.; Turkulets, Y.; Shalish, I.; Jelinek, R. Tungsten-Disulfide/Polyaniline High Frequency Supercapacitors. *Adv. Electron. Mater.* **2021**, *7*, 2100025. [CrossRef]

5. Zeng, R.; Li, Z.C.; Li, L.B.; Li, Y.Z.; Huang, J.; Xiao, Y.B.; Yuan, K.; Chen, Y.W. Covalent Connection of Polyaniline with MoS2 Nanosheets toward Ultrahigh Rate Capability Supercapacitors. *ACS Sustain. Chem. Eng.* **2019**, *7*, 11540–11549. [CrossRef]

6. Sajedi-Moghaddam, A.; Mayorga-Martinez, C.C.; Saievar-Iranizad, E.; Sofer, Z.; Pumera, M. Exfoliated transition metal dichalcogenide (MX_2; M = Mo, W; X = S, Se, Te) nanosheets and their composites with polyaniline nanofibers for electrochemical capacitors. *Appl. Mater. Today* **2019**, *16*, 280–289. [CrossRef]

7. Choi, W.; Choudhary, N.; Han, G.H.; Park, J.; Akinwande, D.; Lee, Y.H. Recent development of two-dimensional transition metal dichalcogenides and their applications. *Mater. Today* **2017**, *20*, 116–130. [CrossRef]

8. Nam, M.S.; Patil, U.; Park, B.; Sim, H.B.; Jun, S.C. A binder free synthesis of 1D PANI and 2D MoS_2 nanostructured hybrid composite electrodes by the electrophoretic deposition (EPD) method for supercapacitor application. *RSC Adv.* **2016**, *6*, 101592–101601. [CrossRef]

9. Joseph, N.; Shafi, P.M.; Bose, A.C. Recent Advances in 2D-MoS_2 and its Composite Nanostructures for Supercapacitor Electrode Application. *Energ. Fuel.* **2020**, *34*, 6558–6597. [CrossRef]

10. Zhao, X.; Ma, X.; Sun, J.; Li, D.H.; Yang, X.R. Enhanced Catalytic Activities of Surfactant-Assisted Exfoliated WS_2 Nanodots for Hydrogen Evolution. *ACS Nano* **2016**, *10*, 2159–2166. [CrossRef] [PubMed]

11. Coleman, J.N.; Lotya, M.; O'Neill, A.; Bergin, S.D.; King, P.J.; Khan, U.; Young, K.; Gaucher, A.; De, S.; Smith, J.R.; et al. Two-Dimensional Nanosheets Produced by Liquid Exfoliation of Layered Materials. *Science* **2011**, *331*, 568–571. [CrossRef] [PubMed]

12. Bhandavat, R.; David, L.; Singh, G. Synthesis of Surface-Functionalized WS_2 Nanosheets and Performance as Li-Ion Battery Anodes. *J. Phys. Chem. Lett.* **2012**, *3*, 1523–1530. [CrossRef]

13. Desai, J.A.; Adhikari, N.; Kaul, A.B. Chemical exfoliation efficacy of semiconducting WS_2 and its use in an additively manufactured heterostructure graphene–WS_2–graphene photodiode. *RSC Adv.* **2019**, *9*, 25805–25816. [CrossRef] [PubMed]

14. Leong, S.X.; Mayorga-Martinez, C.C.; Chia, X.; Luxa, J.; Sofer, Z.; Pumera, M. 2h → 1T Phase Change in Direct Synthesis of WS_2 Nanosheets via Solution-Based Electrochemical Exfoliation and Their Catalytic Properties. *ACS Appl. Mater. Interfaces* **2017**, *9*, 26350–26356. [CrossRef]

15. Huang, F.; Jian, J.K.; Wu, R. Few-layer thick WS_2 nanosheets produced by intercalation/exfoliation route. *J. Mater. Sci.* **2016**, *51*, 10160–10165. [CrossRef]

16. Zhang, M.; Nautiyal, A.; Du, H.; Wei, Z.; Zhang, X.; Wang, R. Electropolymerization of polyaniline as high-performance binder free electrodes for flexible supercapacitor. *Electrochim. Acta* **2021**, *376*, 138037. [CrossRef]

17. Dhandapani, E.; Thangarasu, S.; Ramesh, S.; Ramesh, K.; Vasudevan, R.; Duraisamy, N. Recent development and prospective of carbonaceous material, conducting polymer and their composite electrode materials for supercapacitor-A review. *J. Energy Storage* **2022**, *52*, 104937. [CrossRef]

18. Crisci, M.; Boll, F.; Merola, L.; Pflug, J.J.; Liu, Z.M.; Gallego, J.; Lamberti, F.; Gatti, T. Nanostructured 2D WS_2@PANI nanohybrids for electrochemical energy storage. *Front. Chem.* **2022**, *10*, 1000910. [CrossRef] [PubMed]

19. Abdelnasir, S.; Mungroo, M.R.; Shahabuddin, S.; Siddiqui, R.; Khan, N.A.; Ahmad, I.; Anwar, A. Polyaniline (PANI)-conjugated tungsten disulphide (WS_2) nanoparticles as potential therapeutics against brain-eating amoebae. *Appl. Microbiol. Biot.* **2022**, *106*, 3279–3291. [CrossRef]

20. Basnayaka, P.A.; Ram, M.K.; Stefanakos, L.; Kumar, A. High performance graphene-poly(o-anisidine) nanocomposite for supercapacitor applications. *Mater. Chem. Phys.* **2013**, *141*, 263–271. [CrossRef]

21. Kuwertz, R.; Kirstein, C.; Turek, T.; Kunz, U. Influence of acid pretreatment on ionic conductivity of Nafion® membranes. *J. Membrane. Sci.* **2016**, *500*, 225–235. [CrossRef]

22. Wan, M.; Yang, J. Studies on the structure and electrical properties of poly (ortho-toluidine). *Synth. Met.* **1995**, *73*, 201–204. [CrossRef]

23. Wan, M.; Li, J. Tubular poly(ortho-toluidine) synthesized by a template-free method. *Polym. Adv. Technol.* **2003**, *14*, 320–325. [CrossRef]

24. Ghorai, A.; Midya, A.; Maiti, R.; Ray, S.K. Exfoliation of WS$_2$ in the semiconducting phase using a group of lithium halides: A new method of Li intercalation. *Dalton Trans.* **2016**, *45*, 14979–14987. [CrossRef] [PubMed]

25. Mitioglu, A.A.; Plochocka, P.; Deligeorgis, G.; Anghel, S.; Kulyuk, L.; Maude, D.K. Second-order resonant Raman scattering in single-layer tungsten disulfide WS$_2$. *Phys. Rev. B* **2014**, *89*, 245442. [CrossRef]

26. Lai, Z.C.; He, Q.Y.; Ha Tran, T.H.; Repaka, D.V.M.; Zhou, D.D.; Sun, Y.; Xi, S.B.; Li, Y.X.; Chaturvedi, A.; Tan, C.L.; et al. Metastable 1T′-phase group VIB transition metal dichalcogenide crystals. *Nat. Mater.* **2021**, *20*, 1113–1120. [CrossRef] [PubMed]

27. Agyapong, A.D.; Cooley, K.A.; Mohney, S.E. Reactivity of contact metals on monolayer WS$_2$. *J. Appl. Phys.* **2020**, *128*, 055306. [CrossRef]

28. Shi, W.; Lin, M.L.; Tan, Q.H.; Qiao, X.F.; Zhang, J.; Tan, P.H. Raman and photoluminescence spectra of two-dimensional nanocrystallites of monolayer WS$_2$ and WSe$_2$. *2D Mater.* **2016**, *3*, 025016. [CrossRef]

29. Pagona, G.; Bittencourt, C.; Arenal, R.; Tagmatarchis, N. Exfoliated semiconducting pure 2H-MoS$_2$ and 2H-WS$_2$ assisted by chlorosulfonic acid. *Chem. Commun.* **2015**, *51*, 12950–12953. [CrossRef] [PubMed]

30. Baibarac, M.; Cochet, M.; Łapkowski, M.; Mihut, L.; Lefrant, S.; Baltog, I. SERS spectra of polyaniline thin films deposited on rough Ag, Au and Cu. Polymer film thickness and roughness parameter dependence of SERS spectra. *Synthetic. Met.* **1998**, *96*, 63–70. [CrossRef]

31. Bowen, R.D.; Edwards, H.G.M.; Varnali, T. Influence of a methyl substituent on the Raman spectrum of but-3-enyl methyl ether. *Spectrochim. Acta A* **2012**, *93*, 26–32. [CrossRef] [PubMed]

32. Quillard, S.; Louarn, G.; Lefrant, S.; MacDiarmid, A.G. Vibrational analysis of polyaniline: A comparative study of leucoemeraldine, emeraldine, and pernigraniline bases. *Phys. Rev. B* **1994**, *50*, 12496–12508. [CrossRef] [PubMed]

33. Boyer, M.I.; Quillard, S.; Rebourt, E.; Louarn, G.; Buisson, J.P.; Monkman, A.; Lefrant, S. Vibrational analysis of polyaniline: A model compound approach. *J. Phys. Chem. B* **1998**, *102*, 7382–7392. [CrossRef]

34. Dai, F.W.; Zhuang, Q.Y.; Huang, G.; Deng, H.Z.; Zhang, X. Infrared Spectrum Characteristics and Quantification of OH Groups in Coal. *ACS Omega* **2023**, *8*, 17064–17076. [CrossRef] [PubMed]

35. Li, G.; Zhang, Y.Y.; Li, Q.M.; Wang, C.; Yu, Y.; Zhang, B.B.; Hu, H.S.; Zhang, W.Q.; Dai, D.X.; Wu, G.R.; et al. Infrared spectroscopic study of hydrogen bonding topologies in the smallest ice cube. *Nat. Commun.* **2020**, *11*, 5449. [CrossRef] [PubMed]

36. Golczak, S.; Kanciurzewska, A.; Fahlman, M.; Langer, K.; Langer, J.J. Comparative XPS surface study of polyaniline thin films. *Solid State Ion.* **2008**, *179*, 2234–2239. [CrossRef]

37. Mahat, M.M.; Mawad, D.; Nelson, G.W.; Fearn, S.; Palgrave, R.G.; Payne, D.J.; Stevens, M.M. Elucidating the deprotonation of polyaniline films by X-ray photoelectron spectroscopy. *J. Mater. Chem. C* **2015**, *3*, 7180–7186. [CrossRef]

38. Wu, M.S.; Wen, T.C.; Gopalan, A. Electrochemical copolymerization of diphenylamine and anthranilic acid with various feed ratios. *J. Electrochem. Soc.* **2001**, *148*, D65–D73. [CrossRef]

39. Trchová, M.; Stejskal, J.; Prokeš, J. Infrared spectroscopic study of solid-state protonation and oxidation of polyaniline. *Synthetic. Met.* **1999**, *101*, 840–841. [CrossRef]

40. Cho, W.H.; Cheng, I.C.; Chen, J.Z. Performance Comparison of Reduced Graphene Oxide (rGO)-polyaniline (PANI) Supercapacitors with LiCl, Li$_2$SO$_4$, and H$_2$SO$_4$ Electrolytes. *J. Electrochem. Soc.* **2023**, *170*, 010532. [CrossRef]

41. Yuvika Sood, A.; Lokhande, P.E.; Kadam, V.; Jagtap, C.; Mudila, H.; Rednam, U.; Kumar, D.; Ansar, S.; Kumar, Y.A.; Aepuru, R.; et al. Nanocomposites combining 2D WS2 and 1D polyaniline for enhanced high-performance supercapacitors. *J. Alloys Compd.* **2024**, *1005*, 1760. [CrossRef]

42. Visakh, C.; Mohan, V.; Rakhi, R.B. WS$_2$/Conducting polymer nanocomposite-based flexible and binder-free electrodes for high-performance supercapacitors. *Electrochim. Acta* **2024**, *498*, 144657. [CrossRef]

43. Kozarenko, D.O.; Dyadyun, V.S.; Kotenko, I.E.; Posudievsky, O.Y.; Koshechko, V.G.; Pokhodenko, V.D. Mechanochemically prepared nanocomposites based on polyaniline and molybdenum and tungsten disulfides as electrode materials for supercapacitors. *Theor. Exp. Chem.* **2018**, *54*, 85–91. [CrossRef]

44. Chevulamaddi, H.; Kalagadda, V.R. The improved electrochemical performance of MnO$_2$ nanorods decorated with polyaniline as efficient electrode towards high performance supercapacitors. *J. Mater. Sci. Mater. Electron.* **2024**, *35*, 2273. [CrossRef]

45. Hekmat, F.; Shahrokhian, S.; Taghavinia, N. Ultralight, flexible asymmetric supercapacitors based on manganese dioxide–polyaniline nanocomposite and reduced graphene oxide electrodes directly deposited on foldable cellulose papers. *J. Phys. Chem. C* **2018**, *122*, 27156–27168. [CrossRef]

46. Dadashi, R.; Farhadi, K.; Bahram, M. Polybenzidine-MnO$_2$ nanocomposite on anodized graphite sheet as a novel system for high-performance supercapacitors. *Diam. Relat. Mater.* **2024**, *143*, 110923. [CrossRef]

47.   Zhang, M.; Du, H.; Wei, Z.; Zhang, X.; Wang, R. Facile electrodeposition of Mn-CoP nanosheets on Ni foam as high-rate and ultrastable electrodes for supercapacitors. *ACS Appl. Energy Mater.* **2022**, *5*, 186–195. [CrossRef]

48.   Zhag, M.; Du, H.; Wei, Z.; Zhang, X.; Wang, R. Ultrafast Microwave Synthesis of Nickel-Cobalt Sulfide/Graphene Hybrid Electrodes for High-Performance Asymmetrical Supercapacitors. *ACS Appl. Energy Mater.* **2021**, *4*, 8262–8274. [CrossRef]